Title: A novel redox-active switch in Fructosamine-3-kinases expands the regulatory repertoire of the protein kinase superfamily

Authors: Safal Shrestha[1], Samiksha Katiyar[2], Carlos E. Sanz-Rodriguez[2], Nolan R. Kemppinen[2], Hyun W. Kim[2], Renuka Kadirvelraj[2], Charalampos Panagos[3], Neda Keyhaninejad[5], Maxwell Colonna[2,3], Pradeep Chopra[3], Dominic P. Byrne[6], Geert J. Boons[3,4], Esther V. Knaap[5], Patrick A. Eyers[6], Arthur S. Edison[1,2,3], Zachary A. Wood[2], Natarajan Kannan[1,2]*.

Affiliations:

[1]Institute of Bioinformatics, University of Georgia, Athens, GA. 30602. USA.

[2]Department of Biochemistry and Molecular Biology, University of Georgia, Athens, GA. 30602. USA.

[3]Complex Carbohydrate Research Center (CCRC), University of Georgia, Athens, GA. 30602. USA.

[4]Department of Chemical Biology and Drug Discovery, Utrecht Institute for Pharmaceutical Sciences, and Bijvoet Center for Biomolecular Research, Utrecht University, 3584 CG Utrecht, The Netherlands.

[5]Center for Applied Genetic Technologies (CAGT), University of Georgia, Athens, GA. 30602. USA.

[6]Department of Biochemistry, Institute of Integrative Biology, University of Liverpool, Liverpool, United Kingdom.

[7]Department of Horticulture, University of Georgia, Athens, GA. 30602. USA.

*Correspondence to nkannan@uga.edu

One Sentence Summary: Structural basis for FN3K redox regulation

Abstract (252 words)

Aberrant regulation of metabolic kinases by altered redox homeostasis is a major contributing factor in aging and disease such as diabetes. However, the biochemical mechanisms by which metabolic kinases are regulated under oxidative stress is poorly understood. In this study, we demonstrate that the catalytic activity of a conserved family of Fructosamine-3-kinases (FN3Ks), which are evolutionarily related to eukaryotic protein kinases (ePKs), are regulated by redox active cysteines in the kinase domain. By solving the crystal structure of FN3K homolog from *Arabidopsis thaliana* (AtFN3K), we demonstrate that it forms an unexpected strand-exchange dimer in which the ATP binding P-loop and adjoining beta strands are swapped between two chains in the dimer. This dimeric configuration is characterized by strained inter-chain disulfide bonds that stabilize the P-loop in an extended conformation and tethers the substrate-binding lobes in a unique inactive conformation. Mutational analysis and solution studies confirm that the strained disulfides function as redox "switches" to reversibly regulate FN3K activity and dimerization. Consistently, we find that human FN3K, which contains an equivalent P-loop Cys, is also redox sensitive, whereas ancestral bacterial FN3K homologs, which lack a P-loop Cys, are not. Furthermore, CRISPR knockout of FN3K in human HepG2 cells results in significant upregulation of redox metabolites including glutathione. We propose that redox regulation evolved progressively in FN3Ks in response to changing cellular redox conditions. Our studies provide important new insights into the origin and evolution of redox regulation in the protein kinase superfamily and open new avenues for targeting human FN3K in diabetic complications.

Introduction

Glycation is a universal post-translational modification in which reducing sugars such as glucose and fructose are non-enzymatically added to free amine groups on peptides, proteins and lipids. This non-enzymatic modification occurs endogenously in all living organisms, as well as exogenously in foods we consume (*1*, *2*). Sugars attached to amine groups can undergo Amadori rearrangements to form stable linkages with biomolecules (*3*-*5*). Because such linkages can adversely affect biomolecular functions, organisms have evolved deglycation mechanisms (*6*-*8*) to repair the potential toxic effects of reactive sugars. Fructosamine-3 kinases (FN3Ks) are a conserved family of deglycation enzymes that remove ribose and fructose sugars attached to surface exposed lysine (Lys) residues (ketosamines) in proteins (*9*-*12*). They do this by catalyzing the transfer of the gamma phosphate from ATP to the 3’ hydroxyl group in the ketosamine substrate. Phosphorylation of ketosamines by FN3Ks results in an unstable ketosamine 3-phosphate intermediate, which spontaneously decomposes into inorganic phosphate (*9*). Since the original unmodified Lys is regenerated as a consequence of FN3K deglycation activity, FN3Ks are believed to function as protein repair enzymes (*6*, *13*).

FN3Ks are conserved across the tree of life (Fig. 1A) (*14*). While simple eukaryotes and prokaryotes both contain a single copy of the FN3K gene, complex eukaryotes, including mammals, encode two copies, FN3K and FN3K related protein (FN3K-RP), presumably due to a gene duplication event in amphibians (Fig. 1A). Although the functions of FN3K homologs in lower eukaryotes and bacteria are yet to be equivocally established, it is proposed that they repair proteins modified by ribose-5-phosphate, a potent glycating agent generated by the metabolic pentose phosphate pathway (*6*, *12*, *14*, *15*). While FN3K activity is essential for normal cellular functions, uncontrolled activity can result in altered cellular homeostasis and disease (*16*, *17*). For example, accumulation of 3-deoxyglucosone, a byproduct of human FN3K activity, is a prognostic marker for diabetic complications such as retinopathy and neuropathy (*18, 19*). Increased 3-deoxyglucosone levels also contribute to oxidative stress by inhibiting glutathione peroxidase, a potent cellular antioxidant (*20*). Thus, tight regulation of FN3K activity is crucial to main cellular homeostasis and to prevent oxidative stress resulting from its own repair functions. However, despite the remarkable conservation of FN3Ks across the tree of life and their fundamental roles in cellular functions and disease, a mechanistic understanding of FN3K function and mode(s) of regulation is currently lacking.

We previously showed that FN3Ks belong to a large super-family of protein kinase-like (PKL) enzymes that include eukaryotic protein kinases, small molecule kinases, and atypical kinases (*21*, *22*). FN3Ks are more closely related to small molecule kinases, such as aminoglycoside kinase (APH) and choline kinases, than ePKs and more distantly related to atypical pseudokinases such as Fam20C and SelO (*23-25*). Through quantitative comparisons of the evolutionary constraints acting on diverse PKL-fold enzymes, we previously demonstrated that ePKs share sequence and structural similarity with small molecule kinases in the N-terminal ATP binding lobe, but diverge significantly in the C-terminal substrate binding lobe (*21, 22, 26*). In particular, the extended activation segment connecting the ATP and substrate binding lobes that classically controls catalytic activity through conformational changes driven by reversible phosphorylation of serine, threonine and tyrosine residues (*27*) is unique to ePKs and absent in small molecule kinases, including FN3Ks. An accompanying paper submitted side-by-side with this manuscript demonstrates that in addition to reversible phosphorylation, oxidation and reduction of a conserved Cys residue in the activation segment is a much more common mode of Ser/Thr protein kinase regulation than had been previously appreciated (*28*).

Here, we identify a critical role for the ATP binding P-loop in the redox regulation of FN3Ks. By solving the first crystal structure of a eukaryotic FN3K homolog, *Arabidopsis thaliana* FN3K (AtFN3K), we find that the P-loop is stabilized in an extended conformation by a Cys-mediated disulfide bond connecting two chains to form a covalently linked dimer. We show that reduction of disulfides results in AtFN3K activation. Consistently, the human FN3K (HsFN3K) conserving the P-loop cysteine is redox-active and displays altered oligomerization when proliferating cells are exposed to acute oxidative stress.

We propose that redox control mediated by the P-loop Cys is an ancient mechanism of FN3K regulation that emerged progressively during FN3K evolution from bacteria to humans. Because many protein kinases contain an equivalent redox-active cysteine in the P-loop, our studies also have broad implications for understanding the structure, function and evolution of all PKL-fold enzymes, in particular tyrosine kinases, which contain a cysteine residue at the equivalent position. Our detailed mechanistic characterization of FN3Ks also open new avenues for the design of FN3K-targeted small molecule inhibitors for diabetic complications associated with increased protein glycation.

Results

Crystal structure of AtFn3K reveals a novel strand-exchange dimer

To investigate the structural basis for biological FN3K regulation, we solved the first crystal structure of a plant FN3K homolog (AtFN3K) in complex with the adenosine triphosphate (ATP) mimic Adenylyl-imidodiphosphate (AMP-PNP) at a resolution of 2.37 Å using a multiple model molecular replacement strategy (Table S1). The asymmetric unit of AtFN3K contains two molecules with a small degree of disorder at the N- and C- termini (residues 1-6 and 296, 297) (Fig. 2A). Each chain contains a well-ordered molecule of AMP-PNP in the active site, albeit with missing electron density for γ-phosphate (Fig. 2B). AMP-PNP is known to hydrolyze slowly over time, as shown previously for Protein Kinase A (*29*). Because the nitrogen atom in the β-phosphate of AMP-PNP could not be identified, we have modeled the ligand as ADP.

AtFN3K adopts a canonical protein kinase fold (PKL-fold) with an N-terminal ATP binding lobe and C-terminal substrate binding lobe. A comparison to the bacterial search model (PDB code 5IGS) shows that the chains superimpose 218 Cα atoms with an rmsd of 3.3 Å (*30*). Due to the strong similarity between the two structures and the fact that the closely related aminoglycoside phosphotransferase structure from *E. coli* (5IGS) has already been described in detail (*31*), we focus here on the unique structural features of AtFN3K. Unlike other kinases, the AtFN3K structure is a 'strand-exchange' dimer, in which the β1 strand in one chain forms an anti-parallel β-sheet with the β2 strand of the adjacent chain (Fig. 2C). In most PKL-fold crystal structures solved to date, the β1 strand forms an intra-chain anti-parallel beta sheet with β2, and the P-loop connecting the two strands typically positions the ATP for catalysis, as observed in TfFN3K, aminoglycoside kinase and the prototypic eukaryotic Protein Kinase (ePK) A (Fig. 1B, 3A). However, in the AtFN3K dimer, the P-loop is unfolded, and the extended P-loop conformation is stabilized by an intermolecular disulfide bond between Cys^{32} in chain A and Cys^{32} in chain B (Fig. 2B, 3A). A second intermolecular disulfide is formed between Cys^{236} in each chain (Fig. 2B, 3B). Cys^{236} is located in the F-G loop, which is typically involved in substrate binding in both small molecule kinases and protein kinases (Fig. 3B). In the AtFN3K dimer, the substrate binding lobes are covalently tethered to create a unique interface, presumably for phosphorylating ketosamine and related substrates (Fig. 3C). The AtFN3K dimer buries nearly 2500 Å^2 (16.4%) of solvent accessible area of each monomer. The total solvation free energy (ΔG) gain upon formation of the interface is calculated to be -36.2 kcal/mol (p-value of 0.014) and a total of 36 hydrogen bonds and 2 disulfide bridges are formed at the dimer interface (Fig. S1) (*32*).

Disulfides in the AtFN3K dimer interface are conformationally strained

Disulfide bonds in proteins can be classified into various categories based on their geometry and torsional strain energy (*33-35*). Conformational analysis of inter-molecular disulfides in AtFN3K indicates non-ideal geometry (Figure 4A). In particular, the χ3 dihedral of -112.7° (Cβ-Sγ- Sγ- Cβ) for Cys^{236}-Cys^{236} deviates from the peak distribution of ~90° observed for disulfides in the Protein Data Bank (PDB) (Figure 4B). Likewise, the Cα-Cα distance of 3.8 Å for Cys^{32}-Cys^{32} is much shorter than 5.7 Å peak observed for Cα-Cα distances in the PDB (*36, 37*). These non-ideal geometries suggest that the inter-molecular disulfides, in particular the Cys^{236}-Cys^{236} disulfide, are conformationally strained.

P-loop cysteine is critical for the formation of disulfide linked dimer species

Next, we wanted to test if either or both cysteines are essential for the observed disulfide linked dimer. We mutated the cysteine residues individually and together to alanine residues and subjected them to non-reducing SDS-PAGE analysis in the presence of redox agents, 1,4-

Dithiothreitol (DTT) and H_2O_2. The disulfide linked dimer is absent in the P-loop cysteine mutants (Cys32Ala and Cys32Ala/Cys236Ala) but not in the Cys236Ala mutants (Fig. 5A), suggesting that the P-loop cysteine is critical for the observed disulfide linked dimer. In addition, we identified multiple monomeric species on the gel, including a reduced monomer (M_{Red}) and monomers with intramolecular disulfide (M_{S-S}) (Fig. 5A). The presence of M_{S-S} band in the double cysteine mutant led us to hypothesize that the two remaining cysteines, Cys^{196} and Cys^{222} (Fig. 5B), in the kinase domain could form intramolecular disulfides. To test if an intramolecular disulfide is formed in solution or upon denaturation, we treated the Size Exclusion Chromatography (SEC) purified WT dimer with N-Ethylmaleimide (NEM) before denaturation. NEM blocks free thiols and prevents their oxidation and subsequent disulfide formation (*38*). The absence of M_{S-S} and the presence of M_{Red} in the NEM treated sample suggests that the M_{S-S} band is a consequence of denaturation (Fig. S2). As a control, we also ran a non-reducing SDS page on the triple cysteine mutant (Cys32Ala/Cys236Ala/Cys196Ala), which is incapable of forming any intramolecular disulfides. As expected, only M_{Red} band was observed in the triple mutant (Fig. S2), further suggesting that the M_{S-S} band is a consequence of denaturation during SDS page analysis. For this reason, we primarily focus on the inter-chain disulfides observed in the crystal structure.

AtFN3K WT dimer is activated by redox agents

In order to determine the functional state of the native enzyme (WT) in solution, we performed SEC on the purified protein. Interestingly, we identified two peaks, a dimer and a monomer (Fig. 6A, Fig S3A) with the dimer peak being dominant in solution. The purified dimer resolved on non-reducing SDS-PAGE gel as two distinct bands (Fig. S4). To test sensitivity to DTT, we performed PK/LDH assay on the dimer and monomer fractions in the presence and absence of 2 mM DTT. The activity of the dimer species increased nearly 40fold in the presence of the reductant (Fig. 6B). In contrast, the monomer species was active but insensitive to DTT (Fig. 6B), suggesting that only the dimer species is redox sensitive. We also performed PK/LDH assays on single and double cysteine to alanine or serine mutants. P-loop cysteine (Cys32/Ala/Ser) mutants were less sensitive to DTT compared to C-lobe cysteine mutants (Cys236/Ala/Ser) (Fig. S5A). Moreover, AtFN3K WT also showed sensitivity to DTT when activity was measured independently using Nuclear Magnetic Resonance (NMR)-based assay which measures ribuloselysine phosphorylation (Fig. S5B).

In order to test if AtFN3K could dimerize without the cysteines, we performed SEC on the triple cysteine mutant (Cys32Ala/Cys236Ala/Cys196Ala). Similar to the native enzyme, we identified both dimer and monomer peaks (Fig. 6C). We hypothesized that the two species (monomer and dimer) would be insensitive to DTT since they are incapable of forming cysteine disulfide bridge. As expected, both the dimer and monomer species were insensitive to DTT (Fig. 6D). Taken together, these data suggest that AtFN3K can still dimerize in the absence of two cysteine residues (Cys^{32} and Cys^{236}), which lie in the dimer interface.

To test whether the monomer and dimer species were in equilibrium, we first performed sedimentation velocity analysis on the purified Cys32Ala/Cys236Ala/Cys196Ala triple mutant. c(s) analysis revealed a distribution consisting of a monomer peak at 2.0 S and a dimer peak at 3.1 S which are predicted to be at 2.2 S and 3.6 S, respectively (Fig. S3B). Glycerol is required to maintain the recombinant AtFN3K stably in solution and has a tendency to form a self-gradient during centrifugation which will disproportionately reduce the S-values of sedimenting species. The monomer-dimer distribution is consistent with the size exclusion profile suggesting that the protein exists in two predominant species (Fig 6C, S3A). Secondly, we performed sedimentation velocity analysis across a moderate change (5x) in protein concentration but did not detect any changes in the ratio of monomers and dimers present (Fig. S3B). We then isolated the two species using SEC and performed sedimentation velocity. The dimer sample lacked the monomer peak at 2.0 S and vice versa likely indicating a lack of equilibrium between the two species (Fig. S3C). Together, the data suggest that the dimer and the monomer represent two distinct species that do not exchange under an equilibrium.

Evolution of P-loop cysteine redox regulation

Multiple sequence alignment of FN3K orthologs from diverse organisms indicates that while the P-loop cysteine (Cys^{32}) is conserved across diverse organisms, the other three cysteines (Cys^{236}, Cys^{196} and Cys^{222}) are unique to plant FN3Ks (Fig. 5B). Notably, human FN3K (HsFN3K) and FN3K-RP (HsFN3KRP) both contain an equivalent cysteine in the P-loop. HsFN3K contains three additional cysteines, two of which are specific to both FN3K and FN3K-RP. We expressed and purified HsFN3K and assayed its activity under reducing conditions. The activity of HsFN3K increased in the presence of DTT in a manner similar to that observed for AtFN3K (Fig. 7A). Importantly, mutating the equivalent P-loop cysteine (Cys^{24}) to alanine results in loss of sensitivity to DTT. We also tested the activity in the presence of reduced glutathione (GSH), a physiological reducing agent. The activity increased for the WT whereas no change was observed for the Cys24Ala mutant (Fig. S6A). As a control, we expressed, purified and assayed AtFN3K homologs from *Thermobifida fusca* (TfFN3K) and *Lactobacillus plantarum* (LpFN3K), which contain a histidine and aspartate in place of the P-loop cysteine, respectively (Fig. 5B). Notably, TfFN3K and LpFN3K catalytic activity did not change in the presence of any of the redox agents tested (Fig. 7B). Also, non-reducing SDS PAGE for the WT and Cys24Ala mutant HsFN3K confirmed that the P-loop cysteine is essential for dimerization (Fig. S6B)

Finally, to extend these findings in mammalian cells, we overexpressed Flag-tagged-HsFN3K in HEK293T cells using transient transfection. Cells were grown for 48 hours and treated with different concentrations of diamide. Diamide decreases the cellular concentration of reduced glutathione (GSH) and promotes disulfide formation (*39*). It can also react with free thiols in proteins and lead to disulfide bond formation (*40*). Diamide treatment induced higher order oligomerization of WT HsFN3K, but not the Cys24Ala mutant (Fig. 7C).

FN3K CRISPR knockout alters redox sensitive cellular metabolites

Cellular functions of FN3Ks are currently unknown. Our analysis of FN3K expression in various cancer cell lines identified significant overexpression in liver and eye cancer cells. To assess the functional significance of this increased expression, we generated a Clustered Regularly Interspaced Short Palindromic Repeats (CRISPR) knock out of HsFN3K (FN3K-KO) in HepG2 liver cancer cell line (Fig. S7) and compared the metabolome of WT and FN3K-KO cells using untargeted 1H nuclear magnetic resonance (1H NMR) metabolomics. This revealed significant difference in metabolite abundance in FN3K-KO compared to WT (Fig. 8A, B, Table S2). Of special note, glutathione and lactate levels were increased in FN3K knockout cells relative to wild type HepG2 cells, while pantothenate, phosphocreatine/creatine ratio, aspartate, glycine, and serine levels were decreased. Glutathione is a major cellular redox regulator (*41*), while intracellular levels of pantothenate, glycine, serine and aspartate, are known to be reactive to the redox status of the cell (*42*-*44*). Additionally, phosphocreatine/creatine ratio and lactate control ATP production and glycolysis, respectively (*45*). The enrichment of these metabolites suggests potential links between FN3Ks, redox levels and ATP production.

Discussion

Here we report the structural basis for redox regulation in an ancient family of phosphorylation-based enzymes associated with protein repair. The crystal structure of *Arabidopsis thaliana* FN3K reveals a novel strand exchange dimer in which two chains are covalently linked by disulfide bonds emanating from the P-loop in the ATP binding lobe and F-G loop in the substrate binding lobe. We propose that these disulfide bridges are conformationally strained and are essential for maintaining AtFN3K in an inhibited dimeric conformation. Our studies also show that inhibited native AtFN3K (WT dimer) is activated more than 40-fold under reducing conditions. We speculate that reduction of the disulfides releases the constrain on the P-loop and the substrate binding F-G-loop to allow ATP and substrate access, and catalysis in the dimeric state. Thus, AtFN3K toggles between an inhibited “oxidized” dimer state and active “reduced” dimer to phosphorylate ketosamine substrates. Using SEC, we also identified a monomeric species insensitive to DTT. Although crystallization attempts to isolate the monomeric species have been unsuccessful, we predict that a monomer would adopt a canonical kinase fold without any beta-strand exchange. As a result, both P-loop and substrate binding loops cannot be constrained through disulfide bridges, preventing redox regulation.

Similarly, SEC employed on the Cys32Ala/Cys236Ala/Cys196Ala mutant revealed the presence of both dimeric and monomeric species, indicating that the enzyme can dimerize without these cysteines. PISA analysis of the crystal structure had showed that nearly 2500 Å^2 (16.4%) of each monomer is buried as part of the dimer interface. Sedimentation velocity analysis further revealed that the two species were distinct and did not exist in equilibrium.

Our cellular studies show that dimerization and higher order oligomerization of human FN3K is altered after exposure to the thiol-oxidizing agent, diamide. Consistently, a recent unbiased proteomic study identified a sulfenylated form of the P-loop cysteine in human FN3K-RP in HeLa cells under conditions of oxidative stress (*46*), suggesting that a regulatory mechanism of partial Cys P-loop oxidation to sulfenic acid (which is a reversible modification) is likely to be operative in cells.

The identification of redox active cysteines in FN3Ks also opens up the possibility of a feedback regulation mechanism in which FN3K activity is controlled by its own catalytic byproduct, 3-deoxyglucosone, which is known to contribute to oxidative stress (*20*). We speculate that accumulation of advanced glycation end products such as 3-deoxyglucosone drives the conformational ensemble of FN3K species towards an inactive dimeric form through the oxidation of the P-loop cysteine, while reduced levels maintain FN3K in an active reduced form (Fig. 9A). Such a feedback inhibition mechanism might explain how the essential deglycation functions of FN3K are carried out in cells without contributing to oxidative stress. Consistent with this view, our biochemical and mutational studies confirm that inhibited dimeric species predominate in the absence of reducing agents, while active dimeric or monomeric species may dominate in the presence of reducing agents. Moreover, comparative metabolomics study of the HsFN3K WT and KO in HepG2 liver cells revealed alteration in redox sensitive metabolites, namely glutathione. The increase in cellular glutathione in the KO may suggest that the cells are adapting to oxidative stress caused by the absence of the enzyme. However, this hypothesis needs to be tested in future studies.

Redox control of FN3K may also explain the altered glycated patterns observed in plant and human proteomes (*47-50*) and facilitate deglycation functions to be carried out in different cellular compartments. AtFN3K contains a chloroplast signal peptide N-terminus of the kinase domain, and removal of the signal peptide results in the localization of AtFN3K in different cellular compartments, including nucleus and mitochondria (Fig. S8). Human FN3K-RP is localized in the mitochondria (*51*), and has been detected in red blood cells and serum samples. Because the redox potentials within these cellular compartments are quite different (*52*), the presence of a redox sensitive P-loop cysteine may also help control FN3K activity through subcellular localization. This hypothesis will be tested in future experimental studies that monitor FN3K activity from a variety of subcellular sources.

The P-loop Cys is conserved amongst FN3K orthologs from diverse prokaryotic and eukaryotic organisms, and our studies indicate that the FN3K homolog in human (HsFN3K) is also redox-sensitive. In contrast to the activation loop, which appears to have evolved as a flexible motif for eukaryotic protein kinase regulation by phosphorylation, the P-loop is fundamentally conserved in diverse ATP fold enzymes, where it plays a critical role in clamping ATP and positioning it for efficient catalysis. Protein kinases possess a highly characteristic GlyxGlyxxGly motif in the P-loop that enhances conformational flexibility and permits regulation of ATP binding functions. The P-loop of FN3Ks is characterized by conserved Gly residues in addition to the redox sensitive Cys residue, and based on our structural data, the presence of both these features might be necessary for the strand exchange dimer observed. In this context, it is interesting to note that several tyrosine protein kinases also possess conserved Cys residues embedded within the Gly-rich motifs in the P-loop. These include a Cys at the position equivalent to Cys^{32} of AtFN3K found in eukaryotic SRC, FGFR, YES1 and FYN tyrosine kinases (Fig. 9B). Notably, both SRC and FGFR have previously been shown to be redox-regulated through Cys oxidation mechanisms in the P-loop (*53, 54*). However, whether these kinases also form a strand exchange dimer similar to AtFN3K is not known, and it will be interesting to attempt to solve the structure of Tyr kinases crystallized under different oxidizing conditions.

Finally, human FN3K and FN3K-RP are implicated in human diseases such as diabetic neuropathy and retinopathy, which are associated with increased protein glycation. Both kinases are also highly expressed in human tumors (Fig. S9). However, developing therapeutic strategies for FN3Ks is potentially a double-edged sword because inhibition of FN3K activity can result in the accumulation of glycated proteins, while activation of FN3Ks might result in the accumulation of 3-deoxyglucosone, a potent generator of oxidative stress. Based on our new findings, we propose a combinatorial drug development approach, in which the active monomeric species and the reduced dimeric species are targeted through the development of thiol-interacting agents. These might be developed in order to help normalize cellular protein glycan homeostasis, depending upon the indication and redox balance in the appropriate tissue and the availability of redox-active Cys residues in FN3K targets.

Materials and Methods

Expression and purification of AtFN3K WT and Cys-Ala mutants

AtFN3K inserted into pET-15b expression vector was provided by Prof. Emile Van Shaftingen (Université Catholique of Louvain, Brussels, Belgium). Site directed mutagenesis was performed using Q5 Hot Start High Fidelity Kit from New England Biolabs (NEB). Vectors were transformed into E. coli BL21(DE3) pLysS (Roche) cells and co-expression with GroEL was performed at 16°C for 18 hours in 500 ml of Luria–Bertani medium containing 100 μg/l ampicillin and 25 μg/l chloramphenicol. The bacterial extract was resuspended in 50 mM sodium phosphate buffer, pH 7.8, 300 mM NaCl, 10 % v/v glycerol (Buffer A) with 1mM Phenylmethylsulfonyl Fluoride (PMSF) and 3 mM 2-Mercaptoethanol (βME). The solution was sonicated on ice and the lysate was centrifugated at 15,000 x g for 45 minutes at 4°C. The supernatant was then passed through 0.5 ml of Talon® resin previously equilibrated with Buffer A without βME. The column was washed with 20 ml of Buffer B (50 mM Sodium phosphate buffer, pH 7.8, 1 M NaCl,10 % v/v glycerol) followed by wash with 100 ml of Buffer B containing 10 mM imidazole. The protein was then eluted with Buffer A without βME containing 250 mM Imidazole. The purity of the protein was checked by SDS-PAGE, and the fractions with the protein were dialyzed against buffer A without glycerol and later against Buffer C (25 mM Hepes, pH 7.8, 300 mM NaCl, 10% v/v Glycerol). The protein was snap frozen with liquid nitrogen and stored at -80°C. Recombinant His-HsFN3K was expressed in *E.coli* as well.

Crystallization, phasing and refinement

Recombinant AtFN3K WT was dialyzed into a buffer containing 50 mM NaCl and 15 mM Hepes at pH 8.0, concentrated to ~30 mg/mL and quantified using the extinction coefficient (Abs 0.1%: 1.576) calculated by Protparam (*55*). The protein was crystallized at 20°C using hanging drop vapor diffusion with 2 µl drops (1:1 protein to reservoir ratio). Crystals grew from a reservoir of 2 M ammonium sulfate, 0.1 M MES pH 5.5, 3.28 mM $MgCl_2$ and 1.9 mM AMP-PNP. Crystals were cryoprotected with the reservoir solution supplemented with 10 % cryoprotectant (1:1:1 ratio of ethylene glycol, DMSO, and glycerol) and flash cooled in liquid nitrogen. The diffraction data were collected at the SER-CAT 22-ID beamline at the Argonne National Laboratory using a Rayonix 300HS detector and processed using XDS (*56*). Five percent of the data was set aside for cross validation. The structure was solved by molecular replacement in Phenix (*57*) using a multiple model template (structures from *T. fusca* (PDB code 3F7W), *H. somnus* (PDB code 3JR1) and *E. coli* (PDB code 5IGS) were used) with trimmed side chains and weighted according to structure and homology. Sequence matching and model building was performed using Phenix Autobuild (*57*) . Automated refinement in Phenix (*57*) and iterative manual fitting using Coot (*58*) produced the final model (Table S1). The B-factors were refined using TLS (*59*).

Distribution of $\chi 3$ angle and Cα-Cα distance.

Table S1 titled "Excel spreadsheet of unique disulfides in a culled set of X-ray structures described by G.Wang and R. Dunbrack, Jr." from (*60*) was downloaded and PDBs with resolution less than or equal to 1.5Å was selected to plot the histogram showing the distribution of the $\chi 3$ angle and Cα-Cα distance.

Non-reducing SDS-PAGE

15 µg of the enzyme was incubated with distilled H_2O or redox agents (DTT/H_2O_2) in total volume of 15 µL. After 20 minutes, 5 µL of 4X Sample Buffer without 2-Mercaptoethanol (βME) was added and the protein was denatured at 100˚C for 5 minutes. 10 µL of the sample was loaded onto a 12% SDS-PAGE gel. The gels were stained with Coomassie for an hour and de-stained with water for several hours.

Sequence Alignment

Representative FN3K orthologs were downloaded from Uniprot (*61*), NCBI (*62*) and aligned using MUSCLE (*63*). Eukaryotic protein kinases (ePKs) with P-loop cysteine conserved were identified using previously curated alignment profiles that included ePKs and small molecule kinase sequences including FN3Ks (*21*, *22*, *64*, *65*).

Size Exclusion Chromatography (SEC):

Approximately 4.5 mg of AtFN3K WT and triple cysteine mutants purified using co-expression with GroEL/ES chaperone (9 mg/ml in concentration) was passed through HiLoad 16/1600 Superdex 200 pg column at a flow rate of 1 ml/min with fractionation volume of 1 ml. 25 mM HEPES, pH 7.8, 300 mM NaCl, 10 % v/v glycerol was used as running buffer. SEC was performed at 4 °C. For BSA-Lysozyme standard, 250 µl of 4 mg/ml of BSA and Lysozyme each in running buffer were mixed and loaded on the column. For AtFN3K WT and triple cysteine mutants purified without GroEL/ES chaperone (Fig. S3A), SEC was performed at a flowrate of 0.15 ml/min.

Enzyme Assays

PK/LDH: 1.0 μg (5 μL) of FN3K homologs (At, Tf, Lp)/mutants/dimer and 10 μg (5μL) of HsFN3K, 28 mM of Ribulose-N-α-Ac-lysine (10 μL) in the presence or absence of 20 mM DTT (5 μL) (Final concentration: 2 mM) were mixed with 20 µl of solution prepared by mixing the following: 150 µl of 5X Kinase Buffer (160 mM Hepes, pH 7.4, 80 mM MgCl2, 1.2 M NaCl, 40 % v/v Glycerol), 15 µl of 250 mM Phosphoenolpyruvic acid (PEP), 45 µl of PK/LDH mix [600-100 units/ml pyruvate kinase (PK), 900-1400 units/ml lactic dehydrogenase (LDH)], 90 µl of 37.5 mM Nicotinamide adenine dinucleotide (NADH). The reaction was started by adding 10 μL of 5 mM ATP (final 1mM). The final reaction volume was 50 μL per well. The 96 well plate was immediately placed in a plate reader (Biotek Synergy H4) and the absorbance measured at 340 nm at 35°C continuously for two and half hours. Proteins were stored in Buffer D (25 mM Hepes, pH 7.4, 300 mM NaCl, 10% v/v Glycerol). Buffer D was also used as mock buffer as needed.

NMR real time assay: 100 μg of protein was incubated with 2 mM of ribuloselysine and 600 μM of ATP in 25 mM Hepes, pH 8.0, 5 mM of $MgCl_2$ prepared in D_2O. The reaction was monitored for 50 minutes by acquiring subsequent 1D 1H PURGE (Presaturation Utilizing Relaxation Gradients and Echoes) spectra. All spectra were acquired at 22 °C on an 800 MHz Avance Neo (Bruker) NMR spectrometer equipped with a z-gradient triple resonance TCI cryoprobe and normalized and references using 1H signals of 4,4-dimethyl-4-silapentane-1-

sulfonic acid (DSS). 32 scans were acquired during each experiment with an acquisition time of 1.25 sec. The spectra were processed using NMRpipe and MATLAB.

Sedimentation velocity

Triple cysteine mutant (Cys32Ala/C236Ala/Cys196Ala) were dialyzed into 25 mM HEPES (pH 7.8), 300 mM NaCl, 2 mM $MgCl_2$, 100 μM ATP, and 1 M glycerol, and the protein was quantified using an Agilent 8453 UV/vis with an ε280 of 55810 M-1cm-1 determined by ProtParam (*55*) . The sample was diluted to a final protein concentration of 10 μM then loaded into a 12 mm double-sector Epon centerpieces equipped with quartz windows. The cell was loaded into An60 Ti rotor and equilibrated for 1 hour at 20°C. Sedimentation velocity data were collected using an Optima XLA analytical ultracentrifuge (Beckman Coulter) at a rotor speed of 50000 RPM at 20°C. Data were recorded at 280 nm in radial step sizes of 0.003 cm. SEDNTERP (*66*) was used to model the partial specific volume of AtFN3K (0.713293 mL/g), as well the density (1.0353 g/mL) and the viscosity (0.013277 P) of the buffer. SEDFIT (*67*) was used to analyze the raw sedimentation data. Data were modeled as continuous c(s) distribution and were fit using baseline, meniscus, frictional coefficient, and systematic time-invariant and radial-invariant noise. Fit data for the experiment had an RMSD in the range of 0.005–0.007AU. Predicted sedimentation coefficient (s) values for AtFN3K monomer (2.2 S) and dimer (3.6 S) were calculated from the atomic coordinate of AtFN3K using HYDROPRO (*68*). Data fit and c(s) distribution plots were generated using GUSSI (*69*).

Diamide treatment of HEK293T cells

HEK293T cells were cultured in Dulbecco’s Modified Eagle Media (DMEM) containing 10% Fetal Bovine Serum (FBS) on a 6 cm plate (total 6 plates) and allowed to grow overnight. Cells were transfected with 10 μg of Flag-tagged-HsFN3K (EX-W1392-M46, GeneCopoeia) using Calcium Phosphate Transfection protocol (43). Cells were allowed to grow for 48h. After 48h cells were treated with indicated concentrations of Diamide (Sigma) for 2 h. Cells were lyzed in buffer containing 50 mM Tris.HCl, pH 7.5, 150 mM NaCl, 10% glycerol, 1% TX-100 and 1x protease inhibitor cocktail (EMD-Millipore). Total Cell Lysate (TCL) was spun at 15,000 rpm for 10 min in a refrigerated centrifuge. Proteins were resolved on a 12% SDS-PAGE gel, transferred on PVDF membrane and detected by Western Blotting using anti-Flag antibody (Cell Signaling Technology).

CRISPR Knock Out (KO) cell line and Metabolomics

HepG2 cells were transfected with FN3K Double Nickase Plasmid (sc-412985-NIC) (Santa Cruz Biotechnology) and selected with puromycin according to manufacturer's protocol. FN3K deletion was confirmed by Western Blotting using anti-FN3K antibody (Invitrogen) as shown in Figure S7. Stable cell line stocks were made from single cell colony. Adherent cells were harvested in ice cold 80% methanol extraction solvent and flash frozen in liquid nitrogen. Aqueous metabolites were extracted by vortexing/lysing cell pellets in the extraction solvent and collecting the supernatant. 10% of the supernatant was taken from each sample to form an internal pooled sample. The solvent was then evaporated to produce dried extracts using a CentriVap Benchtop Vacuum Concentrator (Labconco, Kanas City, MO, USA). Extracts were reconstituted in a deuterium oxide phosphate buffer (pH 7.4) prior to data acquisition. 1H NMR) spectra were acquired on all samples using noesypr1d pulse sequence on an 800 MHz Bruker Avance III HD spectrometer. 1H-13C heteronuclear single quantum correlation (1H-13C HSQC) and 1H-1H total correlation spectroscopy (1H-1H TOCSY) spectra were acquired on the internal pooled sample and used for metabolite annotation with COLMARm (*70*). 1H NMR spectra were annotated and analyzed using an in-house MATLAB toolbox to identify significant differences in metabolites between cell lines.

Subcellular Localization

Construction of plasmids for N. benthamiana transformations: For constructs used in the transient assays, full-length wild type or mutant coding sequences (CDS) of AtFN3K were cloned into pENTR/D-TOPO Gateway entry vector (Invitrogen) following the manufacturer's protocol. The coding regions were recombined into binary destination expression vector: pSITE-2CA N-terminal GFP (green fluorescent protein) fusion.

Transient expression of proteins in Nicotiana benthamiana: Agrobacterium tumefaciens strain C58C1 was used for the transient transformation. Colonies carrying the binary plasmids were grown at 28 °C on LB medium plates that contained 50 µg/ml gentamycin and 25 µg/ml rifampicin for selection of the strain, and 100 µg/ml spectinomycin for selection of the binary vector. For agroinfiltration, single colonies were grown overnight in 3 ml LB (28°C, 220 rpm). 50 µl of the agro suspension was added to 5 ml LB and the culture was grown overnight. The agro was pelleted by centrifuging at 4,000 rpm for 20 minutes or 5,0000 rpm for 15 minutes and the suspension was adjusted to an OD_{600} of 0.2-0.3 in infiltration buffer containing 10 mM $MgCl_2$, 10 mM MES, pH 5.7 and 150 mM acetosyringone, pH 5.6, and incubated at room temperature for 3 hours prior to infiltration. To enhance transient expression of the fusion proteins, the viral suppressor of gene silencing p19 protein was co-expressed. For co-infiltration, equal volumes of cultures were mixed and infiltrated into *N. benthamiana* leaves through the abaxial surface using a 1 ml needleless syringe (Becton, Dickinson and Company). Plants were then kept in a growth room at 24/22 °C with a 16/8 hours light/dark photoperiod for 48-72 hrs.

Epifluorescence and confocal microscopy: *N. benthamiana* leaf samples 70 to 90 hours post-infiltration (approximately 0.25 cm2 from the infiltrated area) was mounted in water and viewed directly with a Zeiss LSM 880 confocal scanning microscope using an oil immersion objective 40× Plan-Apochromat 1.4NA (numerical aperture of 1.4). Fluorescence was excited using 488 nm light for GFP. GFP emission fluorescence was selectively detected at 490-540 nm using the Zen 2.3 SP1 software. Each experiment was repeated three times.

Synthesis of Ribulose-N- α -Ac-lysine

A solution of *N*-α-acetyl-L-lysine (0.5 g, 2.66 mmol) and D-ribose (1.6 g, 10.64 mmol) in methanol (100 mL) was stirred at 50°C for 4 h under argon gas. The solvent was evaporated under vacuum and the residue obtained was purified over silica gel column by flash chromatography (R_f = 0.14, EtOAc/MeOH/H_2O, 5/3/2, v/v/v). The product obtained was further purified over a column of Dowex® 50 x 8 H^+ resin (0.6 x 5 cm) cation exchange resin using 150 mM NaCl as an eluent and desalted over a P-2 column using H_2O as an eluent. The desired fractions were combined, concentrated and lyophilized to afford product as white solid (0.55 g, 64.7%); LRMS (ESI): calcd. for C13H25N2O7 $[M+H]^+$ 321.16, found 321.09. Synthesized Ribulose-*N*-α-Ac-lysine was characterized using NMR and ESI (Fig. S10).

Supplementary Materials

Fig. S1. Hydrogen bonds and disulfide bridges between chain A and chain B in AtFN3K WT.

Fig. S2. Oxidized monomeric species are an artifact of the SDS-PAGE gel.

Fig. S3. WT and triple cysteine mutant (Cys32Ala/Cys236Ala/Cys196Ala) exist as two distinct species.

Fig. S4. Reducing and non-reducing SDS-PAGE of AtFN3K WT and triple cysteine mutant (Cys32Ala/Cys236Ala/Cys196Ala) dimer and monomer fractions.

Fig. S5. Effects of thiol reagents on activity of AtFN3K and cysteine mutants.

Fig. S6. P-Loop Cysteine (Cys24) is critical for the formation of disulfide linked dimer in HsFN3K.

Fig. S7. Western blot of HsFN3K Knock Out (KO) in HepG2 cells**.**

Fig. S8. WT and Cys32Ala/Cys236Ala AtFN3K localizes to the nucleus.

Fig. S9. Analysis of FN3K and FN3KRP expression in human tumors.

Fig. S10. Spectral data of Ribulose-N-α-Ac-lysine.

Table S1. Data collection and refinement statistics of WT AtFN3K.

Table S2. Metabolites identified in extracts of WT HepG2 and FN3K-KO cells.

References

1. L. C. Maillard, The action of amino acids on sugar; the formation of melanoidin by a methodic route. *Comptes Ren- dus Hebdomadaires Des Seances De L Academie Des Sci- ences* **154**, 66-68 (1912).
2. M. Teodorowicz, J. van Neerven, H. Savelkoul, Food Processing: The Influence of the Maillard Reaction on Immunogenicity and Allergenicity of Food Proteins. *Nutrients* **9**, (2017); published online EpubAug 04 (10.3390/nu9080835).
3. J. E. Hodge, The Amadori rearrangement. *Adv Carbohydr Chem* **10**, 169-205 (1955).
4. H. F. B. a. P. J. Higgins, Reaction of Monosaccharides with Proteins: Possible Evolutionary Significance. *Science* **213**, 222-224 (1981).
5. J. W. Baynes, N. G. Watkins, C. I. Fisher, C. J. Hull, J. S. Patrick, M. U. Ahmed, J. A. Dunn, S. R. Thorpe, The Amadori product on protein: structure and reactions. *Prog Clin Biol Res* **304**, 43-67 (1989).
6. F. C. Emile Van Schaftingen, Elsa Wiame, Maria Veiga-da-Cunha, Enzymatic repair of Amadori products. *Amino Acids* **42**, 1143-1150 (2012).
7. J. B. Veronika Maria Deppe, Timithy O'Connell, Karl-Heinz Maurer, Friedhelm Meinhardt, Enzymatic deglycation of Amadori products in bacteria:mechanisms, occurrence and physiology functions. *Applied Microbiology Biotechnology* **90**, 399-406 (2011).
8. P. G. a. M. Böhm, Advanced glycation end products. Key players in skin aging? *Dermato-Endocrinology* **4**, 259-270 (2012).
9. G. D. François Collard, Vincent Stroobant, Gert Matthijs, Emil Van Shaftingen, A Mammalian Protein Homologous to Fructosamine-3-Kinase Acting on Psicosamines and Ribulosamines but not on Fructosamines. *Diabetes* **52**, 2888-2895 (2003).
10. M. H. R. Ghislain Delpierre, François Collard, Vincent Stroobant, Florent Vanstapel, Helena Santos, and Emile Van Schaftingen, Identification, Cloning, and Heterologous Expression of a Mammalian Fructosamine-3-Kinase. *Diabetes* **49**, 1627-1634 (2000).
11. S. H. Benjamin S. Szwerglod, and Paul J. Beisswenger, Human Fructosamine-3-Kinase. Purification, Sequencing, Substrate Specificity, and Evidence of Activity In Vivo. *Diabetes* **50**, 2139-2147 (2001).
12. R. G. Juliette Fortpied, Vincent Stroobant and Emile van Schaftingen, Plant ribulosamine/erythrulosamine 3-kinase, a putative protein-repair enzyme. *Biochemical Journal* **388**, 795-802 (2005).
13. P. J. B. James R. Conner, Benjamin S. Szwergold, The expression of the genes for fructosamine-3-kinase and fructosamine-3-kinase-related protein appears to be constitutive and unaffected by environmental signal. *Biochemical and Biophysical Research Communications* **323**, 932-936 (2004).
14. G. D. Jérôme Delplanque, Fred R, Opperdoes, and Emile Van Schaftingen, Tissue Distribution and Evolution of Fructosamine 3-Kinase and Fructosamine 3-Kinase-related Protein. *The Journal of Biological Chemistry* **279**, 46606-46613 (2004).
15. J. F. Rita Gemayel, Rim Rzem, Didier Vertommen, Maria Veiga-da-Cunha and Emile Van Schaftingen, May fructosamine 3kinase homologues in bacteria are ribulosamine/erythrulosamine 3-kinase potentially involved in protein deglycation. *The FEBS Journal* **274**, 4360-4374 (2007).
16. B. S. T. R. Brown, K.A. Brown, M.A. Schwartz, A.M. Tobia and F. Kappler, Modulation of in vivo 3-deoxyglucosone levels. *Biochemical Society Transactions* **31**, 1433-1437 (2003).
17. M. V.-d.-C. S. M. A. Pascal, P. Gilon, E. Van Schaftingen, and J. C. Jonas, Effects of fructosamine-3-kinase deficiency on function and survival of mouse pancreatic islets prolonged culture in high glucose or ribose concentrations. *American Journal of Physiology - Endocrinology and Metabolism* **298**, E586-E596 (2010).
18. H. Kusunoki, S. Miyata, T. Ohara, B.-F. Liu, A. Uriuhara, H. Kojima, K. Suzuki, H. Miyazaki, Y. Yamashita, K. Inaba, M. Kasuga, Relation Between Serum 3-Deoxyglucosone and Development of Diabetic Microangiopathy. *Diabetes Care* **26**, 1889 (2003)10.2337/diacare.26.6.1889).
19. T. Niwa, N. Takeda, H. Yoshizumi, A. Tatematsu, M. Ohara, S. Tomiyama, K. Niimura, Presence of 3-Deoxyglucosone, a Potent Protein Crosslinking Intermediate of Maillard Reaction, in Diabetic Serum. *Biochemical and Biophysical Research Communications* **196**, 837-843 (1993); published online Epub1993/10/29/ (https://doi.org/10.1006/bbrc.1993.2325).
20. T. Niwa, S. Tsukushi, 3-deoxyglucosone and AGEs in uremic complications: inactivation of glutathione peroxidase by 3-deoxyglucosone.
21. N. Kannan, S. S. Taylor, Y. Zhai, J. C. Venter, G. Manning, Structural and functional diversity of the microbial kinome. *PLoS Biol* **5**, e17 (2007); published online EpubMar (06-PLBI-RA-0837R2 [pii]

10.1371/journal.pbio.0050017).
22. K. Oruganty, E. E. Talevich, A. F. Neuwald, N. Kannan, Identification and classification of small molecule kinases: insights into substrate recognition and specificity. *BMC Evol Biol* **16**, 7 (2016); published online EpubJan 06 (10.1186/s12862-015-0576-x).
23. V. S. Tagliabracci, S. E. Wiley, X. Guo, L. N. Kinch, E. Durrant, J. Wen, J. Xiao, J. Cui, K. B. Nguyen, J. L. Engel, J. J. Coon, N. Grishin, L. A. Pinna, D. J. Pagliarini, J. E. Dixon, A Single Kinase Generates the Majority of the Secreted Phosphoproteome. *Cell* **161**, 1619-1632 (2015)10.1016/j.cell.2015.05.028).
24. A. Sreelatha, S. S. Yee, V. A. Lopez, B. C. Park, L. N. Kinch, S. Pilch, K. A. Servage, J. Zhang, J. Jiou, M. Karasiewicz-Urbańska, M. Łobocka, N. V. Grishin, K. Orth, R. Kucharczyk, K. Pawłowski, D. R. Tomchick, V. S. Tagliabracci, Protein AMPylation by an Evolutionarily Conserved Pseudokinase. *Cell* **175**, 809-821.e819 (2018); published online Epub2018/10/18/ (https://doi.org/10.1016/j.cell.2018.08.046).
25. A. Kwon, S. Scott, R. Taujale, W. Yeung, K. J. Kochut, P. A. Eyers, N. Kannan, Tracing the origin and evolution of pseudokinases across the tree of life. *Science Signaling* **12**, eaav3810 (2019)10.1126/scisignal.aav3810).
26. N. Kannan, A. F. Neuwald, Did protein kinase regulatory mechanisms evolve through elaboration of a simple structural component? *J Mol Biol* **351**, 956-972 (2005); published online EpubSep 2 (S0022-2836(05)00726-6 [pii]
10.1016/j.jmb.2005.06.057).
27. B. Nolen, S. Taylor, G. Ghosh, Regulation of Protein Kinases: Controlling Activity through Activation Segment Conformation. *Molecular Cell* **15**, 661-675 (2004).
28. D. P. Byrne, S. Shrestha, M. Galler, M. Cao, L. Daly, C. E. Eyers, E. A.Veal, N. Kannan, P. A. Eyers (2020) An evolutionary-conserved redox regulatory mechanism in Ser/Thr protein kinases. Science Signaling *Under Review*
29. A. C. Bastidas, J. M. Deal Ms Fau - Steichen, Y. Steichen Jm Fau - Guo, J. Guo Y Fau - Wu, S. S. Wu J Fau - Taylor, S. S. Taylor, Phosphoryl transfer by protein kinase A is captured in a crystal lattice.
30. L. Holm, P. Rosenström, Dali server: conservation mapping in 3D. *Nucleic acids research* **38**, W545-W549 (2010)10.1093/nar/gkq366).
31. D. H. Fong, D. L. Burk, J. Blanchet, A. Y. Yan, A. M. Berghuis, Structural Basis for Kinase-Mediated Macrolide Antibiotic Resistance.
32. E. Krissinel, K. Henrick, Inference of macromolecular assemblies from crystalline state.
33. B. Schmidt, L. Ho, P. J. Hogg, Allosteric Disulfide Bonds. *Biochemistry* **45**, 7429-7433 (2006); published online Epub2006/06/01 (10.1021/bi0603064).
34. N. Haworth, L. L Feng, M. Wouters, *High torsional energy disulfides: Relationship between cross-strand disulfides and right-handed staples*. (2006), vol. 4, pp. 155-168.
35. M. A. Wouters, S. W. Fan, N. L. Haworth, Disulfides as Redox Switches: From Molecular Mechanisms to Functional Significance. *Antioxidants & Redox Signaling* **12**, 53-91 (2009); published online Epub2010/01/01 (10.1089/ars.2009.2510).
36. N. Srinivasan, R. Sowdhamini, C. Ramakrishnan, P. Balaram, Conformations of disulfide bridges in proteins. *International Journal of Peptide and Protein Research* **36**, 147-155 (1990); published online Epub1990/08/01 (10.1111/j.1399-3011.1990.tb00958.x).
37. G. T. Hanson, D. Aggeler R Fau - Oglesbee, M. Oglesbee D Fau - Cannon, R. A. Cannon M Fau - Capaldi, R. Y. Capaldi Ra Fau - Tsien, S. J. Tsien Ry Fau - Remington, S. J. Remington, Investigating mitochondrial redox potential with redox-sensitive green fluorescent protein indicators.
38. J. D. Gregory, The Stability of N-Ethylmaleimide and its Reaction with Sulfhydryl Groups. *Journal of the American Chemical Society* **77**, 3922-3923 (1955); published online Epub1955/07/01 (10.1021/ja01619a073).
39. N. S. Kosower, E. M. Kosower, in *Methods in Enzymology*. (Academic Press, 1995), vol. 251, pp. 123-133.
40. N. S. Kosower, E. M. Kosower, in *Methods in Enzymology*. (Academic Press, 1987), vol. 143, pp. 264-270.
41. G. Ferrer-Sueta, B. Manta, H. Botti, R. Radi, M. Trujillo, A. Denicola, Factors affecting protein thiol reactivity and specificity in peroxide reduction. *Chem Res Toxicol* **24**, 434-450 (2011); published online EpubApr 18 (10.1021/tx100413v).
42. I. Gout, Coenzyme A, protein CoAlation and redox regulation in mammalian cells. *Biochemical Society transactions* **46**, 721-728 (2018)10.1042/BST20170506).
43. I. Amelio, F. Cutruzzola, A. Antonov, M. Agostini, G. Melino, Serine and glycine metabolism in cancer.

44. J. Garcia-Bermudez, L. Baudrier, K. La, X. G. Zhu, J. Fidelin, V. O. Sviderskiy, T. Papagiannakopoulos, H. Molina, M. Snuderl, C. A. A.-O. h. o. o. Lewis, R. L. A.-O. h. o. o. Possemato, K. A.-O. h. o. o. Birsoy, Aspartate is a limiting metabolite for cancer cell proliferation under hypoxia and in tumours.
45. C. H. Fiske, Y. Subbarow, The Nature of the "Inorganic Phosphate" in Voluntary Muscle. *Science* **65**, 401-403 (1927); published online EpubApr 22 (10.1126/science.65.1686.401).
46. S. Akter, L. Fu, Y. Jung, M. L. Conte, J. R. Lawson, W. T. Lowther, R. Sun, K. Liu, J. Yang, K. S. Carroll, Chemical proteomics reveals new targets of cysteine sulfinic acid reductase. *Nature chemical biology* **14**, 995-1004 (2018); published online Epub2018/11/01 (10.1038/s41589-018-0116-2).
47. T. Bilova, E. Lukasheva, D. Brauch, U. Greifenhagen, G. Paudel, E. Tarakhovskaya, N. Frolova, J. Mittasch, G. U. Balcke, A. Tissier, N. Osmolovskaya, T. Vogt, L. A. Wessjohann, C. Birkemeyer, C. Milkowski, A. Frolov, A Snapshot of the Plant Glycated Proteome: STRUCTURAL, FUNCTIONAL, AND MECHANISTIC ASPECTS. *J Biol Chem* **291**, 7621-7636 (2016); published online EpubApr 01 (10.1074/jbc.M115.678581).
48. U. Greifenhagen, J. Nguyen Vd Fau - Moschner, A. Moschner J Fau - Giannis, A. Giannis A Fau - Frolov, R. Frolov A Fau - Hoffmann, R. Hoffmann, Sensitive and site-specific identification of carboxymethylated and carboxyethylated peptides in tryptic digests of proteins and human plasma.
49. R. Schmidt, D. Bohme D Fau - Singer, A. Singer D Fau - Frolov, A. Frolov, Specific tandem mass spectrometric detection of AGE-modified arginine residues in peptides.
50. Q. Zhang, A. A. Tang N Fau - Schepmoes, L. S. Schepmoes Aa Fau - Phillips, R. D. Phillips Ls Fau - Smith, T. O. Smith Rd Fau - Metz, T. O. Metz, Proteomic profiling of nonenzymatically glycated proteins in human plasma and erythrocyte membranes.
51. P. J. Thul, L. Åkesson, M. Wiking, D. Mahdessian, A. Geladaki, H. Ait Blal, T. Alm, A. Asplund, L. Björk, L. M. Breckels, A. Bäckström, F. Danielsson, L. Fagerberg, J. Fall, L. Gatto, C. Gnann, S. Hober, M. Hjelmare, F. Johansson, S. Lee, C. Lindskog, J. Mulder, C. M. Mulvey, P. Nilsson, P. Oksvold, J. Rockberg, R. Schutten, J. M. Schwenk, Å. Sivertsson, E. Sjöstedt, M. Skogs, C. Stadler, D. P. Sullivan, H. Tegel, C. Winsnes, C. Zhang, M. Zwahlen, A. Mardinoglu, F. Pontén, K. von Feilitzen, K. S. Lilley, M. Uhlén, E. Lundberg, A subcellular map of the human proteome. *Science* **356**, eaal3321 (2017)10.1126/science.aal3321).
52. Y.-M. Go, D. P. Jones, Redox compartmentalization in eukaryotic cells. *Biochimica et biophysica acta* **1780**, 1273-1290 (2008)10.1016/j.bbagen.2008.01.011).
53. D. J. Kemble, G. Sun, Direct and specific inactivation of protein tyrosine kinases in the Src and FGFR families by reversible cysteine oxidation. *Proceedings of the National Academy of Sciences* **106**, 5070 (2009)10.1073/pnas.0806117106).
54. D. E. Heppner, C. M. Dustin, C. Liao, M. Hristova, C. Veith, A. C. Little, B. A. Ahlers, S. L. White, B. Deng, Y.-W. Lam, J. Li, A. van der Vliet, Direct cysteine sulfenylation drives activation of the Src kinase. *Nature Communications* **9**, 4522 (2018); published online Epub2018/10/30 (10.1038/s41467-018-06790-1).
55. E. Gasteiger, C. Hoogland, A. Gattiker, S. e. Duvaud, M. R. Wilkins, R. D. Appel, A. Bairoch, in *The Proteomics Protocols Handbook*, J. M. Walker, Ed. (Humana Press, Totowa, NJ, 2005), pp. 571-607.
56. W. Kabsch, XDS. *Acta Crystallographica Section D* **66**, 125-132 (2010)doi:10.1107/S0907444909047337).
57. P. D. Adams, P. V. Afonine, G. Bunkoczi, V. B. Chen, I. W. Davis, N. Echols, J. J. Headd, L.-W. Hung, G. J. Kapral, R. W. Grosse-Kunstleve, A. J. McCoy, N. W. Moriarty, R. Oeffner, R. J. Read, D. C. Richardson, J. S. Richardson, T. C. Terwilliger, P. H. Zwart, PHENIX: a comprehensive Python-based system for macromolecular structure solution. *Acta Crystallographica Section D* **66**, 213-221 (2010)doi:10.1107/S0907444909052925).
58. P. Emsley, B. Lohkamp, W. G. Scott, K. Cowtan, Features and development of Coot. *Acta Crystallogr D Biol Crystallogr* **66**, 486-501 (2010); published online EpubApr (10.1107/S0907444910007493).
59. A. Urzhumtsev, P. V. Afonine, P. D. Adams, TLS from fundamentals to practice. *Crystallography reviews* **19**, 230-270 (2013)10.1080/0889311X.2013.835806).
60. E. Pijning Aster, J. Chiu, X. Yeo Reichelle, W. H. Wong Jason, J. Hogg Philip, Identification of allosteric disulfides from labile bonds in X-ray structures. *Royal Society Open Science* **5**, 171058 (2018); published online Epub2018/02/01 (10.1098/rsos.171058).
61. T. UniProt Consortium, UniProt: the universal protein knowledgebase. *Nucleic Acids Research* **46**, 2699-2699 (2018)10.1093/nar/gky092).
62. N. A. O'Leary, M. W. Wright, J. R. Brister, S. Ciufo, D. Haddad, R. McVeigh, B. Rajput, B. Robbertse, B. Smith-White, D. Ako-Adjei, A. Astashyn, A. Badretdin, Y. Bao, O. Blinkova, V. Brover, V. Chetvernin, J.

Choi, E. Cox, O. Ermolaeva, C. M. Farrell, T. Goldfarb, T. Gupta, D. Haft, E. Hatcher, W. Hlavina, V. S. Joardar, V. K. Kodali, W. Li, D. Maglott, P. Masterson, K. M. McGarvey, M. R. Murphy, K. O'Neill, S. Pujar, S. H. Rangwala, D. Rausch, L. D. Riddick, C. Schoch, A. Shkeda, S. S. Storz, H. Sun, F. Thibaud-Nissen, I. Tolstoy, R. E. Tully, A. R. Vatsan, C. Wallin, D. Webb, W. Wu, M. J. Landrum, A. Kimchi, T. Tatusova, M. DiCuccio, P. Kitts, T. D. Murphy, K. D. Pruitt, Reference sequence (RefSeq) database at NCBI: current status, taxonomic expansion, and functional annotation. *Nucleic Acids Research* **44**, D733-D745 (2016)10.1093/nar/gkv1189).

63. R. C. Edgar, MUSCLE: multiple sequence alignment with high accuracy and high throughput. *Nucleic Acids Research* **32**, 1792-1797 (2004)10.1093/nar/gkh340).
64. D. I. McSkimming, S. Dastgheib, T. R. Baffi, D. P. Byrne, S. Ferries, S. T. Scott, A. C. Newton, C. E. Eyers, K. J. Kochut, P. A. Eyers, N. Kannan, KinView: a visual comparative sequence analysis tool for integrated kinome research. *Mol Biosyst* **12**, 3651-3665 (2016); published online EpubNov 15 (10.1039/c6mb00466k).
65. R. D. Finn, J. Mistry, J. Tate, P. Coggill, A. Heger, J. E. Pollington, O. L. Gavin, P. Gunasekaran, G. Ceric, K. Forslund, L. Holm, E. L. Sonnhammer, S. R. Eddy, A. Bateman, The Pfam protein families database. *Nucleic Acids Res* **38**, D211-222 (2010); published online EpubJan (gkp985 [pii]10.1093/nar/gkp985 [doi]).
66. T. M. Laue, Computer-aided interpretation of analytical sedimentation data for proteins. *Analytical Ultracentrifugation in Biochemistry and Polymer Science*, 90-125 (1992); published online Epub1992 (
67. P. Schuck, On the analysis of protein self-association by sedimentation velocity analytical ultracentrifugation.
68. A. Ortega, J. Amoros D Fau - Garcia de la Torre, J. Garcia de la Torre, Prediction of hydrodynamic and other solution properties of rigid proteins from atomic- and residue-level models.
69. C. A. Brautigam, Calculations and Publication-Quality Illustrations for Analytical Ultracentrifugation Data.
70. K. Bingol, D.-W. Li, B. Zhang, R. Brüschweiler, Comprehensive Metabolite Identification Strategy Using Multiple Two-Dimensional NMR Spectra of a Complex Mixture Implemented in the COLMARm Web Server. *Analytical Chemistry* **88**, 12411-12418 (2016); published online Epub2016/12/20 (10.1021/acs.analchem.6b03724).
71. D. H. Fong, A. M. Berghuis, Substrate promiscuity of an aminoglycoside antibiotic resistance enzyme via target mimicry. *The EMBO Journal* **21**, 2323 (2002)10.1093/emboj/21.10.2323).
72. J. Zheng, E. A. Trafny, D. R. Knighton, N. Xuong, S. S. Taylor, L. F. Ten Eyck, J. M. Sowadski, 2.2 A refined crystal structure of the catalytic subunit of cAMP-dependent protein kinase complexed with MnATP and a peptide inhibitor. *Acta Crystallographica Section D* **49**, 362-365 (1993)doi:10.1107/S0907444993000423).
73. R. L. Grossman, A. P. Heath, V. Ferretti, H. E. Varmus, D. R. Lowy, W. A. Kibbe, L. M. Staudt, Toward a Shared Vision for Cancer Genomic Data.
74. K. Diederichs, P. A. Karplus, Improved R-factors for diffraction data analysis in macromolecular crystallography.
75. P. A. Karplus, K. Diederichs, Linking crystallographic model and data quality.

Acknowledgments: This work was initially supported by National Science Foundation (NSF) funds to Kannan lab (MCB-1149106) and more recently by National Institute of Health (NIH) (R01GM114409) Pump-priming grant from the University of Georgia and University of Liverpool. Additional support for DPB and PAE was received from a Royal Society Research Grant and North West Cancer Research (CR1208). The staff at the Southeast Regional Collaborative Access Team (SER-CAT) at the Advanced Photon Source is acknowledge. **Author**

contributions: NK conceived and designed the project. SS and SK performed the experiments. CEZ contributed to mutational analysis. DB and PAE contributed reagents and analyzed redox data. NRK, RK and ZAW contributed to X-ray crystallography and structural analysis. HWK collected and analyzed sedimentation velocity data. CP and ASE contributed to NMR studies. SK, MC and ASE contributed to the metabolomics studies. NK and EVK contributed to localization studies on AtFN3K. PC and G-JB contributed to synthesis and purification of ribulose lysine. NK and SS wrote the manuscript with contributions from all authors.

Competing interests: There are no competing interests. **Data and materials availability**: All data associated with this article are either publicly available or included in the article. Structural coordinate and structure factors are made available in the Protein Data Bank (PDB code 6OID).

Figure Legends

Fig. 1. **FN3K adopts a Protein Kinase fold. (A)** FN3Ks are conserved across all the domains of life. **(B)** Overall fold of TfFN3K (PDBID: 3F7W), APH (PDBID: 1L8T) and PKA (PDBID: 1ATP) shown in cartoon representation. The N lobe is colored in light blue and the C lobe in olive. The phosphorylated substrates are shown as either sticks or cartoons, and colored green. The hydroxyl group oxygen atom where phosphate is transferred in each substrate is colored in red.

Fig. 2. AtFN3K WT is a novel beta-strand exchange disulfide mediated dimer. (A) Cartoon representation of the crystal structure of *A. thaliana* FN3K (AtFN3K) homodimer. The two disulfide bridges between two Cys^{32} and two Cys^{236} as well as the ADP molecules are shown as sticks. **(B)** Zoomed in view of simulated annealing omit map (Cys to Ala mutation) as well as the ADP molecule associated with chain B colored in green and contoured at 4.5 rmsd. **(C)** Top view of AtFN3K showing the beta-strand exchange.

Fig. 3. Comparison of AtFN3K ATP and substrate binding region with APH and PKA. (A) Comparison of the AtFN3K P-Loop with Aminoglycoside phosphotranferase (APH) (1L8T) (*71*) and Protein Kinase A (PKA) (1ATP) (*72*). Carbon atoms of ADP and ATP molecules are colored in black. Chain A and Chain B of AtFN3K are colored in slate and salmon respectively. **(B)** Comparison of the substrate binding lobe of AtFN3K with APH(1L8T) (*71*) and PKA (1ATP) (*72*). Kanamycin and peptide substrates are shown as sticks and colored in magenta. **(C)** Surface representation of AtFN3K. Chain A and chain B are colored in slate and salmon respectively. ADP molecule is shown in spheres with carbon atoms colored in black. The two disulfide bridges, C32-C32 and C236-C236 are shown as sticks.

Fig. 4. Geometric analysis of the disulfides in AtFN3K. (A) Distances and dihedral values are labelled for the disulfide bridges between Cys^{32}-Cys^{32} and Cys^{236}-Cys^{236} between chain A and chain B. The angle (Cβ-Sγ-Sγ) is shown with a green dashed line. The dihedrals are shown with dashed line colored in black. **(B)** Distribution of the Cα- Cα distance and χ3 angle (Cβ-Sγ- Sγ- Cβ) for PDB structures with resolution less than 1.5 Å. Values for the Cys^{32}-Cys^{32} and Cys^{236}-Cys^{236} disulfides in AtFN3K is represented by a vertical line colored in magenta.

Fig. 5. P-loop cysteine (Cys32) is critical for the formation of disulfide linked dimer species. (A) Non-reducing SDS-PAGE of AtFN3K WT and Cys to Ala mutants. 15 µg of protein was incubated with 1 mM DTT or 1mM H2O2 for 20 minutes and was then subjected to SDS PAGE under non-reducing conditions. $D_{S\text{-}S}$: Disulfide linked dimer; M_{Red}: Monomer Reduced; MS-S: Monomer with intramolecular disulfide. **(B)** Multiple sequence alignment of FN3K orthologs. Two additional cysteines (Cys^{196} and Cys^{222}) specific to plant FN3Ks are shown. The alignment was generated using MUSCLE.

Fig. 6. Both WT and triple cysteine mutant (Cys32Ala/Cys236Ala/Cys196Ala) exists as two distinct species in solution with the WT dimer being redox sensitive. (A) Size Exclusion Chromatography (SEC) of AtFN3K WT protein. **(B)** Activity of WT protein in the presence and absence of 2 mM DTT. (C) Size Exclusion Chromatography (SEC) of the triple cysteine mutant protein. (D) Activity of WT protein in the presence and absence of 2 mM DTT. **(A, C)** Each fraction was 1 ml in volume. A: Aggregates, D: Dimer, M: Monomer. **(B, D)** 1 µg of protein was assayed using PK/LDH assay as mentioned in the methods. Ribulose-N-α-Ac-lysine was used as the substrate. Error bar represents the standard error of six independent experiments.

Fig. 7. P-loop cysteine is responsible for enzyme redox-sensitivity in HsFN3K. (A) HsFN3K is sensitive to DTT. **(B)** TfFN3K and LpFN3K are insensitive to DTT. **(A, B)** PK/LDH assay was performed with 10.0 µg of HsFN3K and 1.0 µg of TfFN3K and LpFN3K and incubated with buffer (0 mM DTT) or 2 mM DTT. Ribulose-N-α-Ac-lysine was used as the substrate. Error bar indicates the standard error of three independent experiments. **(C)** Effect of different diamide concentrations on overexpressed Flag Tagged HsFN3K WT and C24A in HEK293 cells. D_{S-S}: Dimer, M: Monomer.

Fig. 8. **Redox sensitive metabolites are altered in HsFN3K Crispr knockout. (A)** 1H NMR spectra of HepG2 (WT) and FN3K-KO cells. Traces are the average for each group (HepG2 n=10, FN3K-KO n=9). Insets highlight examples of regions containing annotated metabolites observed to be significantly different between cell lines. **(B)** Box and whisker plots of significant (FDR pvalue < 0.05) metabolites annotated with highest confidence. Black points indicate outliers.

Fig. 9. Proposed redox feedback mechanism in FN3K. (A) Cartoon showing the possible relationship between redox regulation of FN3K activity and its physiological function. The disulfide is colored in yellow. **(B)** Multiple sequence alignment showing all eukaryotic Protein Kinases (ePKs) with a P-loop Cys conserved in the same position as AtFN3K.

Figures

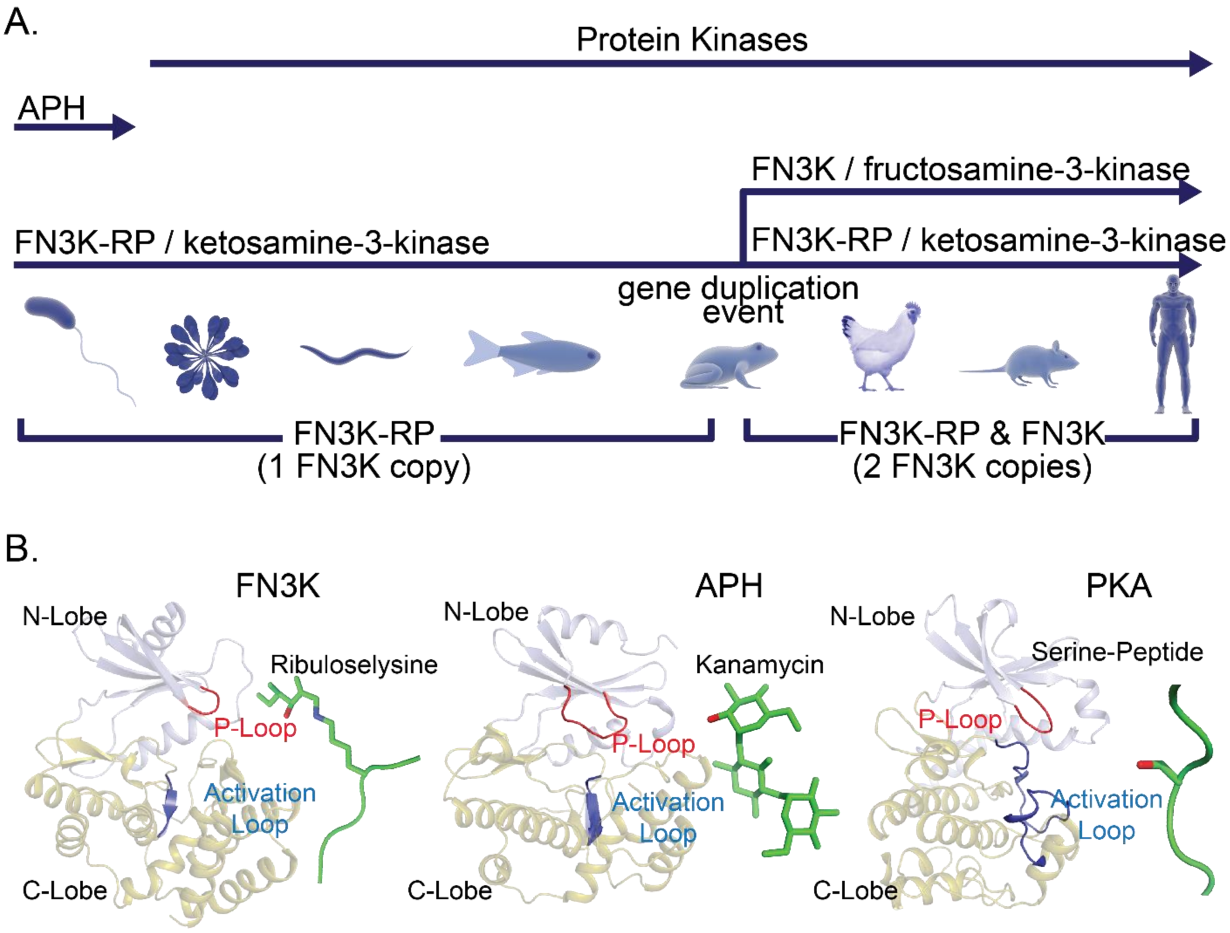

Fig. 1. FN3K adopts a Protein Kinase fold. (A) FN3Ks are conserved across all the domains of life. **(B)** Overall fold of TfFN3K (PDBID: 3F7W), APH (PDBID: 1L8T) and PKA (PDBID: 1ATP) shown in cartoon representation. The N lobe is colored in light blue and the C lobe in olive. The phosphorylated substrates are shown as either sticks or cartoons, and colored green. The hydroxyl group oxygen atom where phosphate is transferred in each substrate is colored in red.

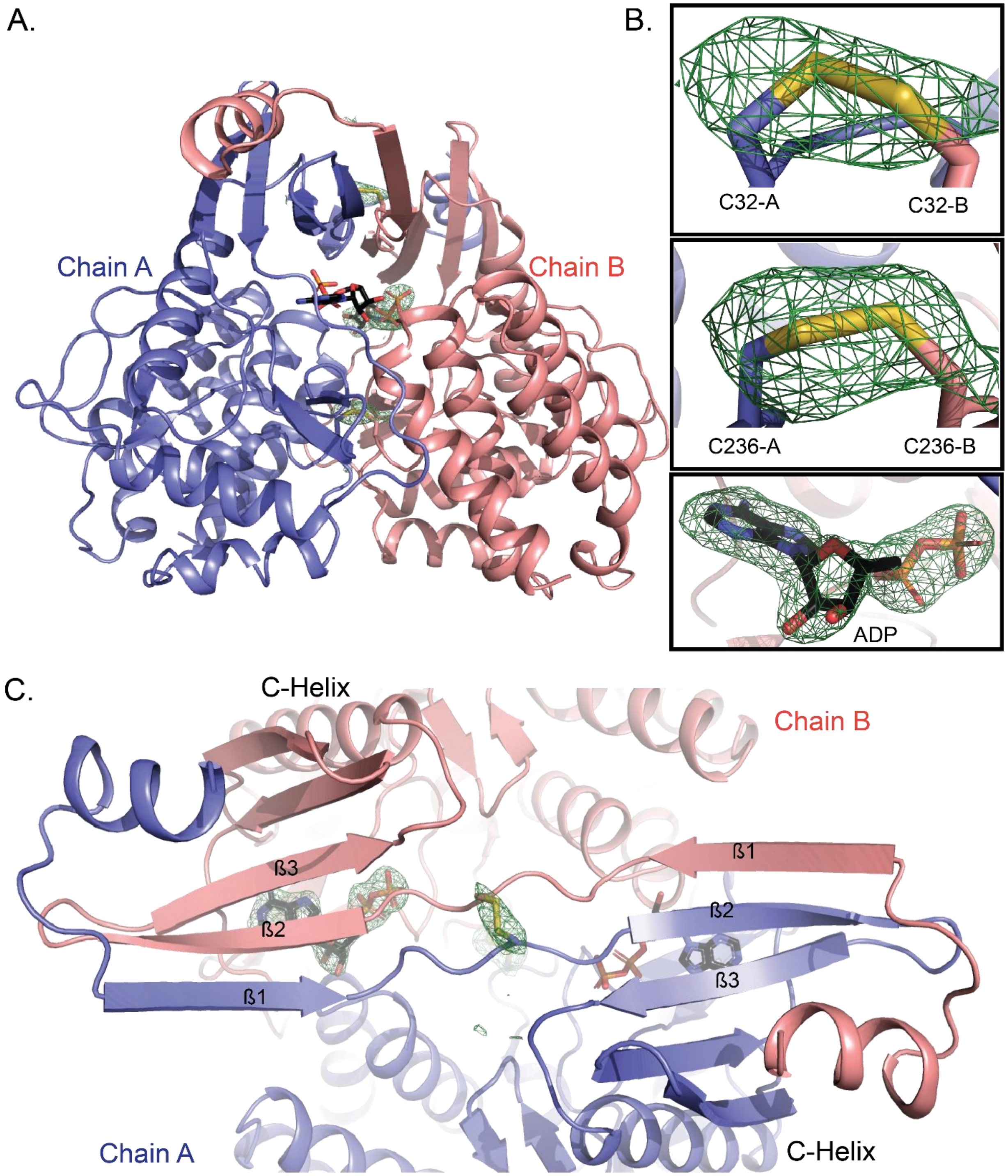
A.
B.
Chain A
Chain B
C32-A
C32-B
C236-A
C236-B
ADP
C.
C-Helix
Chain B
ß3
ß1
ß2
ß2
ß3
ß1
Chain A
C-Helix

Fig. 2. AtFN3K WT is a novel beta-strand exchange disulfide mediated dimer. (A) Cartoon representation of the crystal structure of *A. thaliana* FN3K (AtFN3K) homodimer. The two disulfide bridges between two Cys^{32} and two Cys^{236} as well as the ADP molecules are shown as sticks. **(B)** Zoomed in view of simulated annealing omit map (Cys to Ala mutation) as well as the ADP molecule associated with chain B colored in green and contoured at 4.5 rmsd. **(C)** Top view of AtFN3K showing the beta-strand exchange.

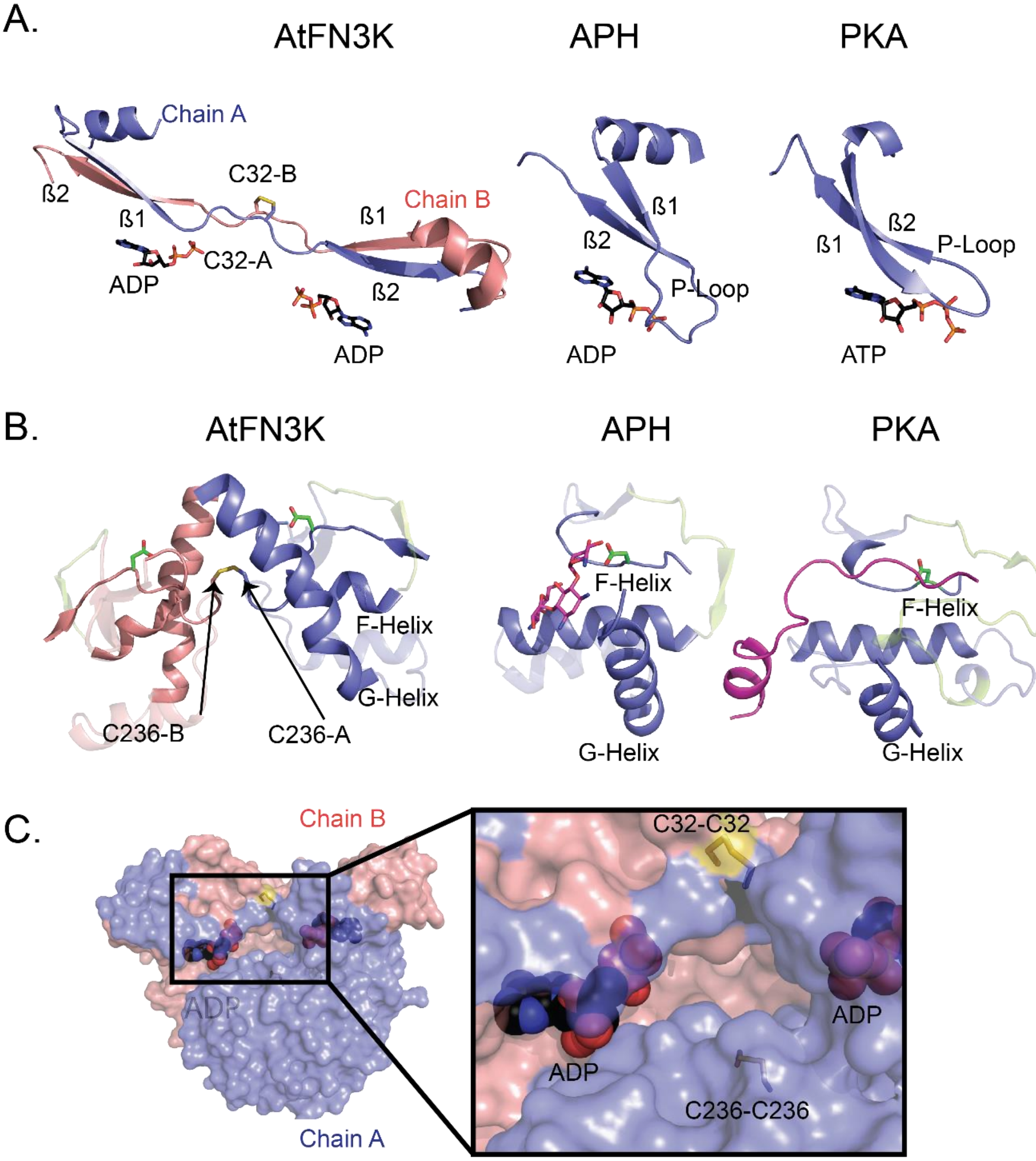

Fig. 3. Comparison of AtFN3K ATP and substrate binding region with APH and PKA. (A) Comparison of the AtFN3K P-Loop with Aminoglycoside phosphotranferase (APH) (1L8T) (*71*) and Protein Kinase A (PKA) (1ATP) (*72*). Carbon atoms of ADP and ATP molecules are colored in black. Chain A and Chain B of AtFN3K are colored in slate and salmon respectively. **(B)**

Comparison of the substrate binding lobe of AtFN3K with APH(1L8T) (*71*) and PKA (1ATP) (*72*). Kanamycin and peptide substrates are shown as sticks and colored in magenta. **(C)** Surface representation of AtFN3K. Chain A and chain B are colored in slate and salmon respectively. ADP molecule is shown in spheres with carbon atoms colored in black. The two disulfide bridges, C32-C32 and C236-C236 are shown as sticks.

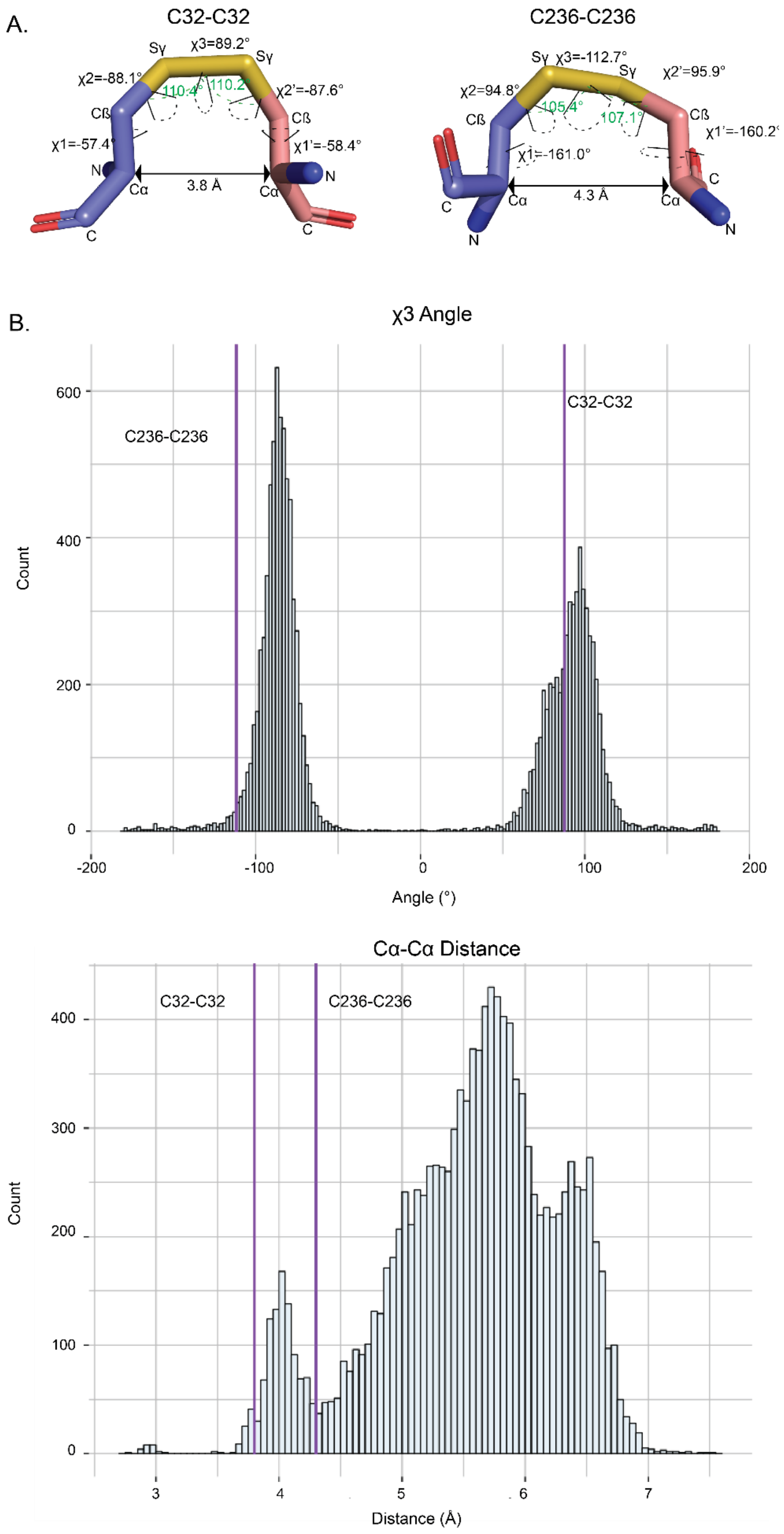
A.
C32-C32
Sγ
χ3=89.2°
Sγ
χ2=-88.1°
110.4°
110.2°
χ2'=-87.6°
Cß
Cß
χ1=-57.4°
χ1'=-58.4°
N
Cα
3.8 Å
Cα
N
C
C
C236-C236
Sγ
χ3=-112.7°
Sγ
χ2'=95.9°
χ2=94.8°
105.4°
107.1°
Cß
Cß
χ1'=-160.2°
χ1=-161.0°
C
Cα
4.3 Å
Cα
C
N
N
B.
χ3 Angle
C236-C236
C32-C32
Count
600
400
200
0
-200
-100
0
100
200
Angle (°)
Cα-Cα Distance
C32-C32
C236-C236
Count
400
300
200
100
0
3
4
5
6
7
Distance (Å)

Fig. 4. Geometric analysis of the disulfides in AtFN3K. (A) Distances and dihedral values are labelled for the disulfide bridges between Cys^{32}-Cys^{32} and Cys^{236}-Cys^{236} between chain A and chain B. The angle (Cβ-Sγ-Sγ) is shown with a green dashed line. The dihedrals are shown with dashed line colored in black. **(B)** Distribution of the Cα- Cα distance and χ3 angle (Cβ-Sγ- Sγ- Cβ) for PDB structures with resolution less than 1.5 Å. Values for the Cys^{32}-Cys^{32} and Cys^{236}-Cys^{236} disulfides in AtFN3K is represented by a vertical line colored in magenta.

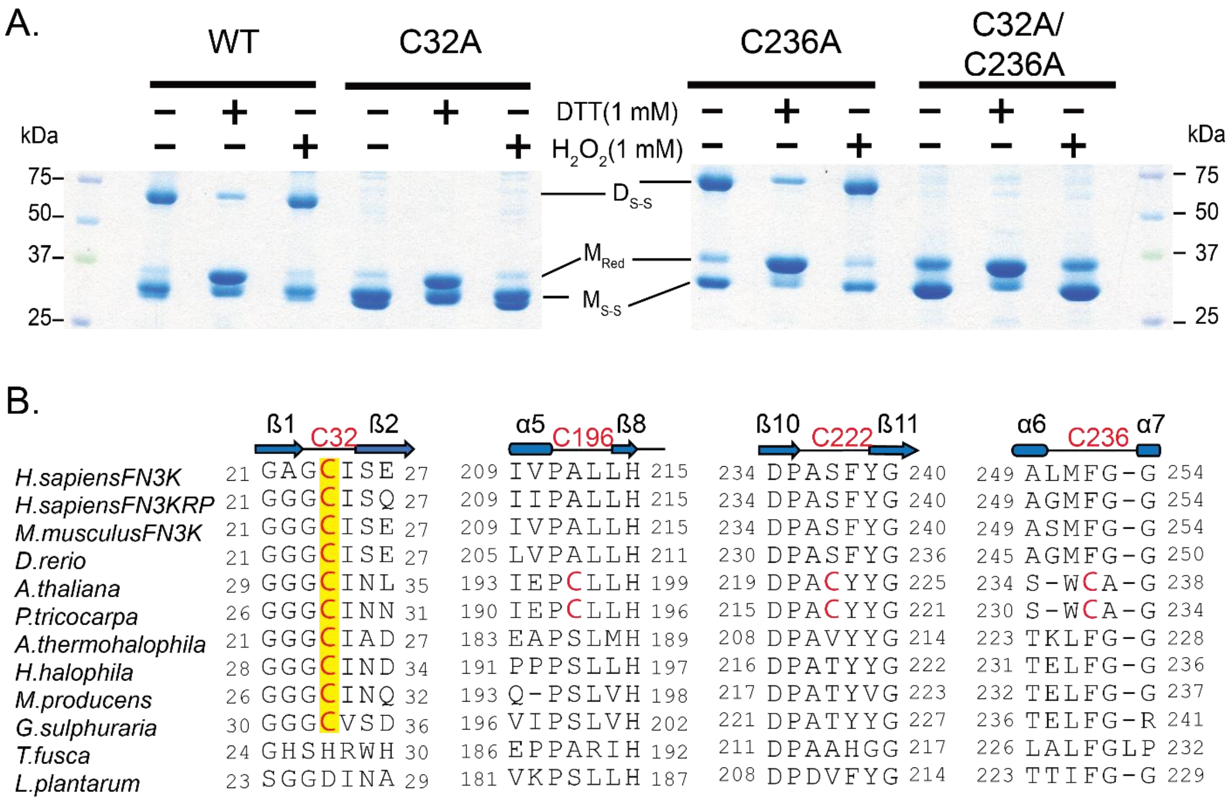

Fig. 5. P-loop cysteine (Cys32) is critical for the formation of disulfide linked dimer species.

(A) Non-reducing SDS-PAGE of AtFN3K WT and Cys to Ala mutants. 15 µg of protein was incubated with 1 mM DTT or 1mM H_2O_2 for 20 minutes and was then subjected to SDS PAGE under non-reducing conditions. D_{S-S}: Disulfide linked dimer; M_{Red}: Monomer Reduced; M_{S-S}: Monomer with intramolecular disulfide. **(B)** Multiple sequence alignment of FN3K orthologs. Two additional cysteines (Cys196 and Cys222) specific to plant FN3Ks are shown. The alignment was generated using MUSCLE.

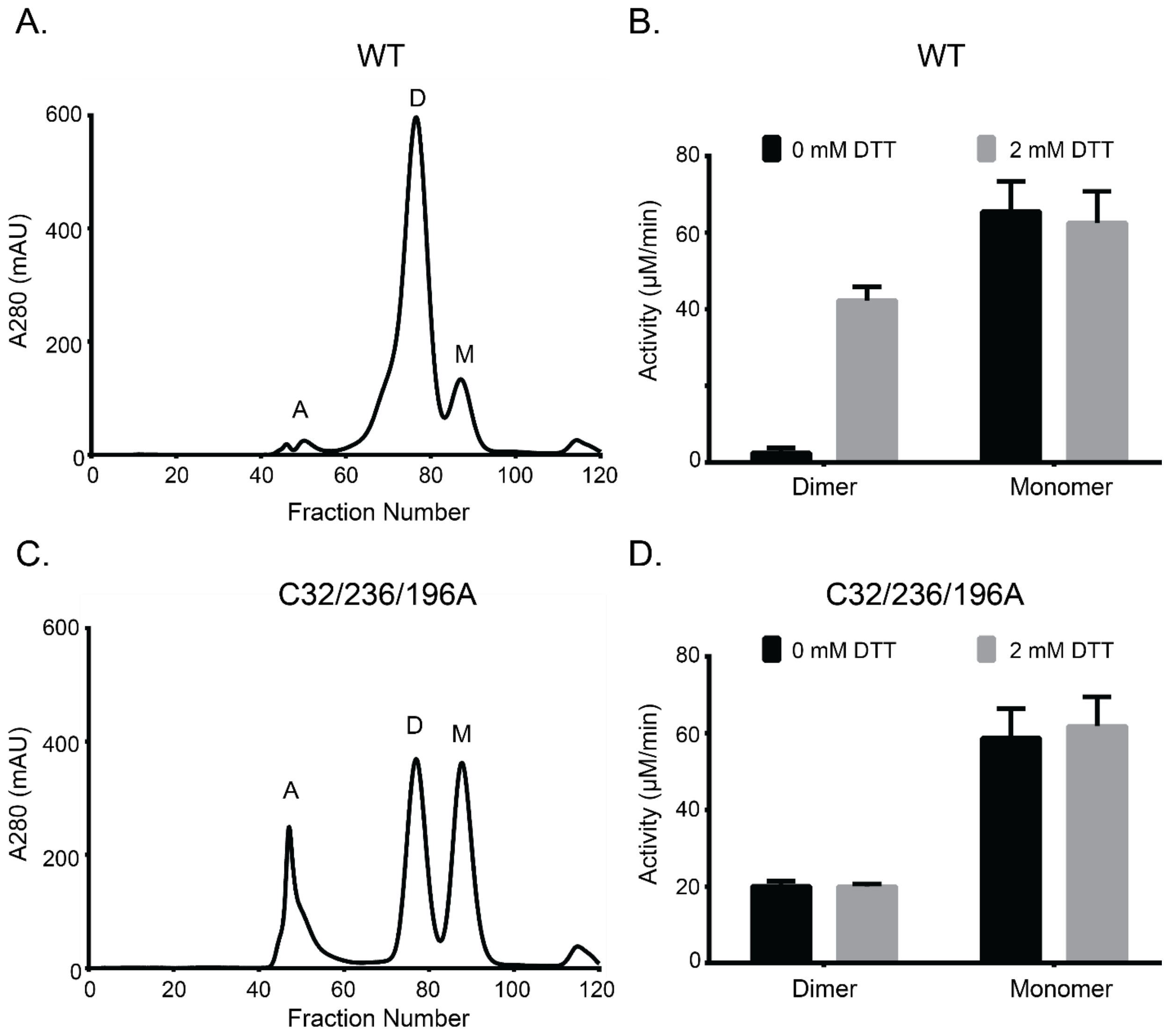

Fig. 6. Both WT and triple cysteine mutant (Cys32Ala/Cys236Ala/Cys196Ala) exists as two distinct species in solution with the WT dimer being redox sensitive. (A) Size Exclusion Chromatography (SEC) of AtFN3K WT protein. **(B)** Activity of WT protein in the presence and absence of 2 mM DTT. **(C)** Size Exclusion Chromatography (SEC) of the triple cysteine mutant protein. **(D)** Activity of WT protein in the presence and absence of 2 mM DTT. **(A, C)** Each fraction was 1 ml in volume. A: Aggregates, D: Dimer, M: Monomer. **(B, D)** 1 µg of protein was assayed using PK/LDH assay as mentioned in the

methods. Ribulose-N-α-Ac-lysine was used as the substrate. Error bar represents the standard error of six independent experiments.

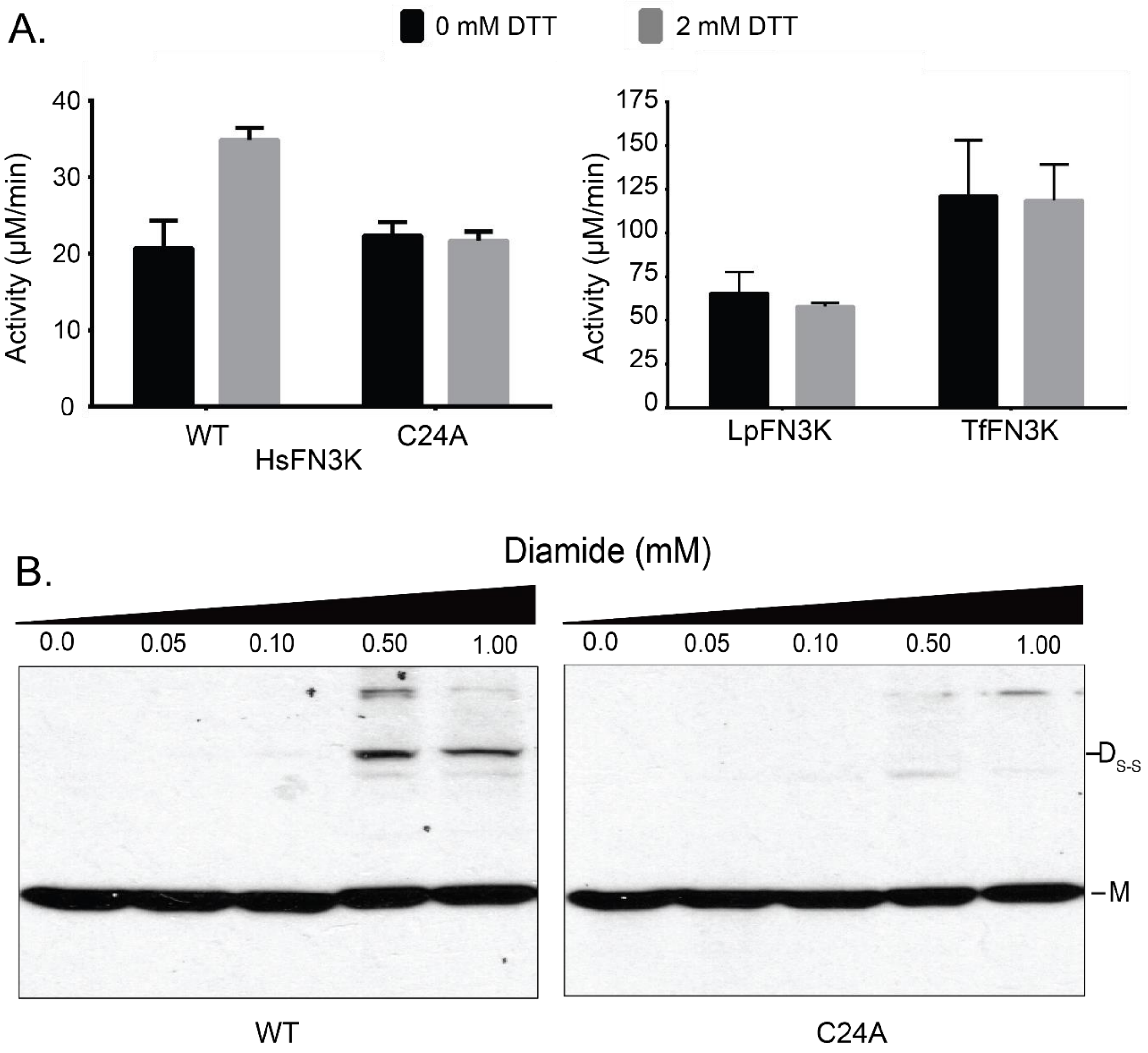

Fig. 7. P-loop cysteine is responsible for enzyme redox-sensitivity in HsFN3K. (A) HsFN3K is sensitive to DTT. **(B)** TfFN3K and LpFN3K are insensitive to DTT. **(A, B)** PK/LDH assay was performed with 10.0 µg of HsFN3K and 1.0 µg of TfFN3K and LpFN3K and incubated with buffer (0 mM DTT) or 2 mM DTT. Ribulose-N-α-Ac-lysine was used as the substrate. Error bar indicates the standard error of three independent experiments. **(C)** Effect of different diamide concentrations on overexpressed Flag Tagged HsFN3K WT and C24A in HEK293 cells. D_{S-S}: Dimer, M: Monomer.

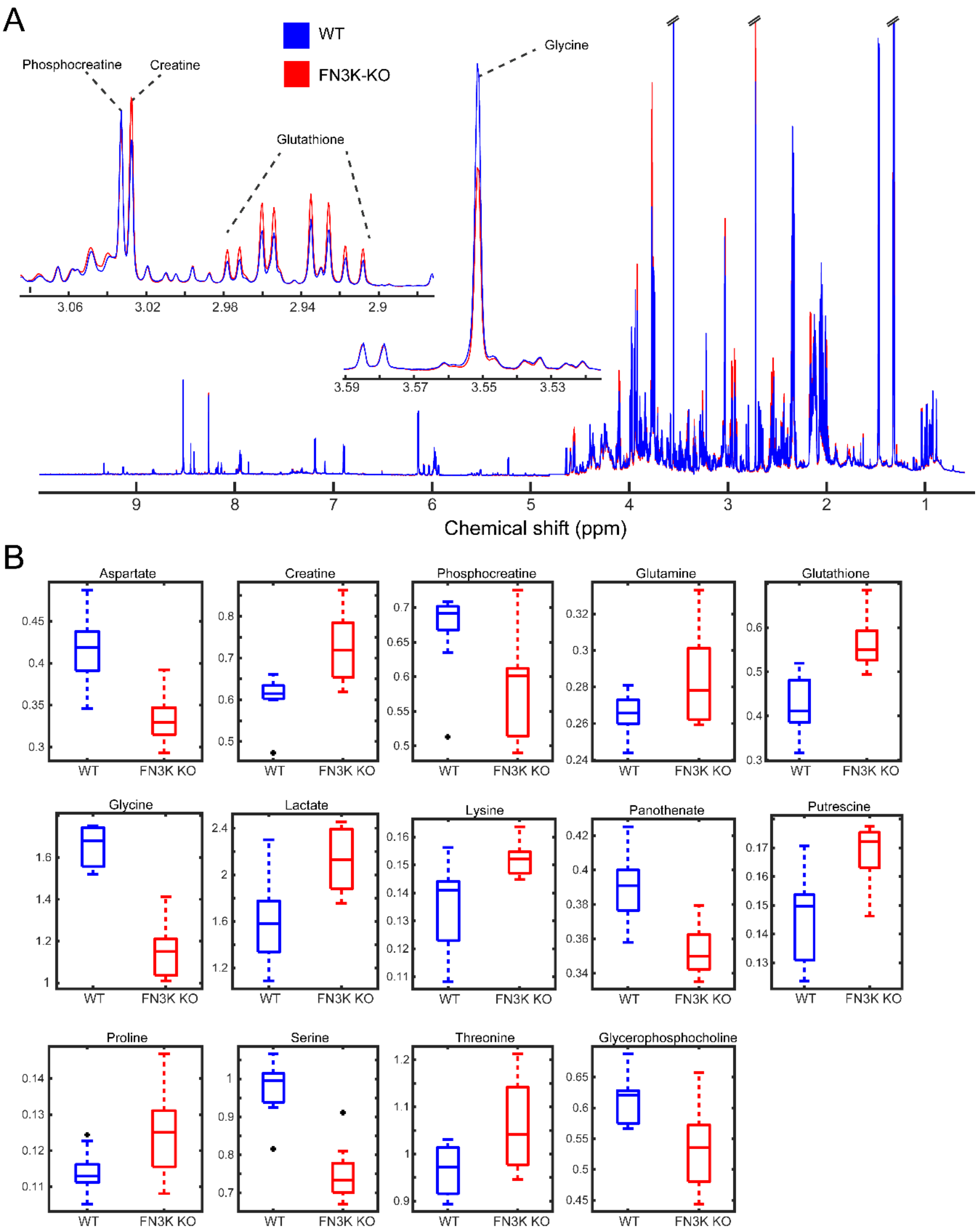
A
🟦 WT
🟥 FN3K-KO
Phosphocreatine
Creatine
Glutathione
Glycine
3.06
3.02
2.98
2.94
2.9
3.59
3.57
3.55
3.53
9
8
7
6
5
4
3
2
1
Chemical shift (ppm)
B
Aspartate
Creatine
Phosphocreatine
Glutamine
Glutathione
Glycine
Lactate
Lysine
Panothenate
Putrescine
Proline
Serine
Threonine
Glycerophosphocholine
WT
FN3K KO

Fig. 8. **Redox sensitive metabolites are altered in HsFN3K Crispr knockout. (A)** 1H NMR spectra of HepG2 (WT) and FN3K-KO cells. Traces are the average for each group (HepG2 n=10, FN3K-KO n=9). Insets highlight examples of regions containing annotated metabolites observed to be significantly different between cell lines. **(B)** Box and whisker plots of significant (FDR pvalue < 0.05) metabolites annotated with highest confidence. Black points indicate outliers.

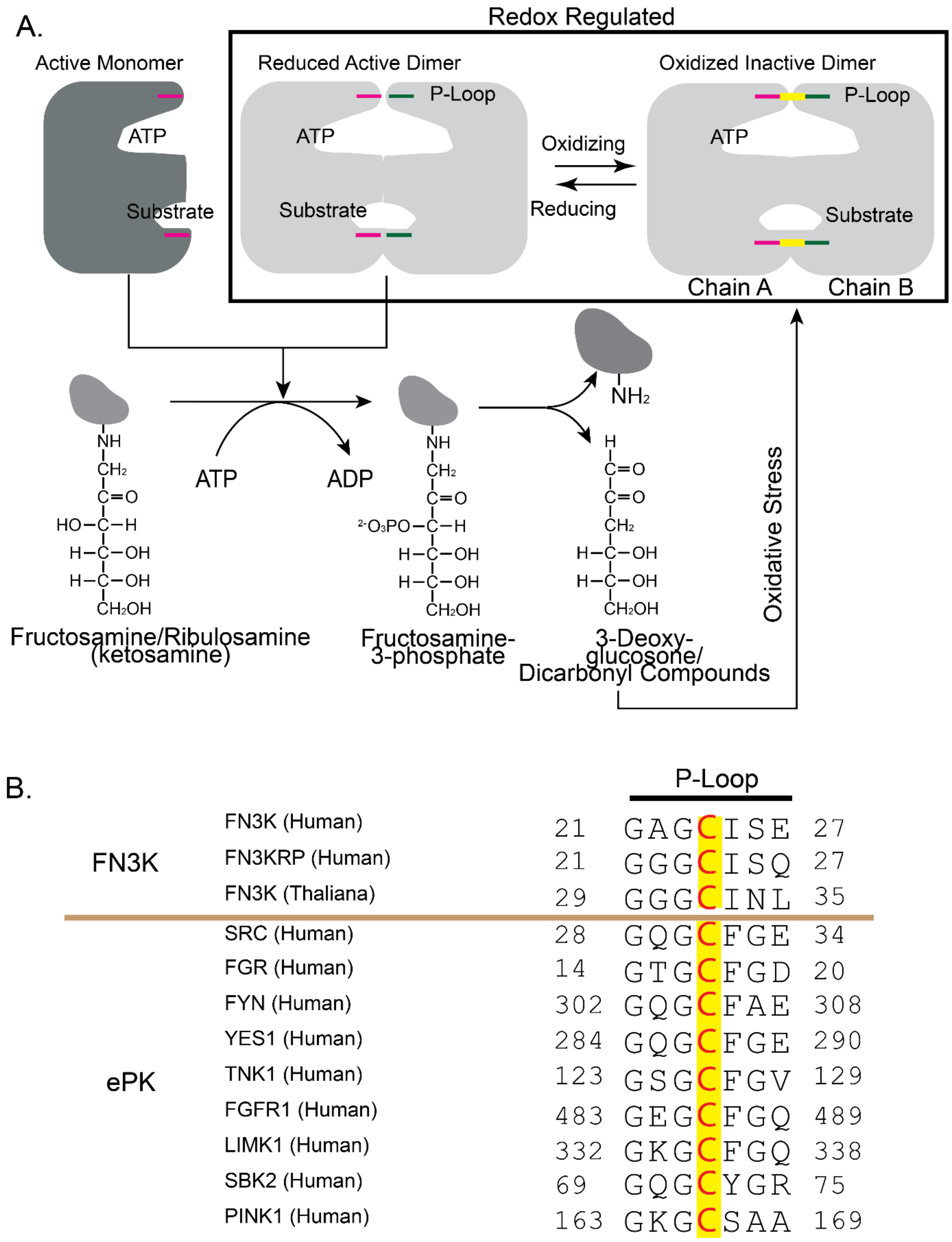

			P-Loop	
FN3K	FN3K (Human)	21	GAGCISE	27
	FN3KRP (Human)	21	GGGCISQ	27
	FN3K (Thaliana)	29	GGGCINL	35
ePK	SRC (Human)	28	GQGCFGE	34
	FGR (Human)	14	GTGCFGD	20
	FYN (Human)	302	GQGCFAE	308
	YES1 (Human)	284	GQGCFGE	290
	TNK1 (Human)	123	GSGCFGV	129
	FGFR1 (Human)	483	GEGCFGQ	489
	LIMK1 (Human)	332	GKGCFGQ	338
	SBK2 (Human)	69	GQGCYGR	75
	PINK1 (Human)	163	GKGCSAA	169

Fig. 9. Proposed redox feedback mechanism in FN3K. (A) Cartoon showing the possible relationship between redox regulation of FN3K activity and its physiological function. The disulfide is colored in yellow. (**B**) Multiple sequence alignment showing all eukaryotic Protein Kinases (ePKs) with a P-loop Cys conserved in the same position as AtFN3K.

Supplementary Materials

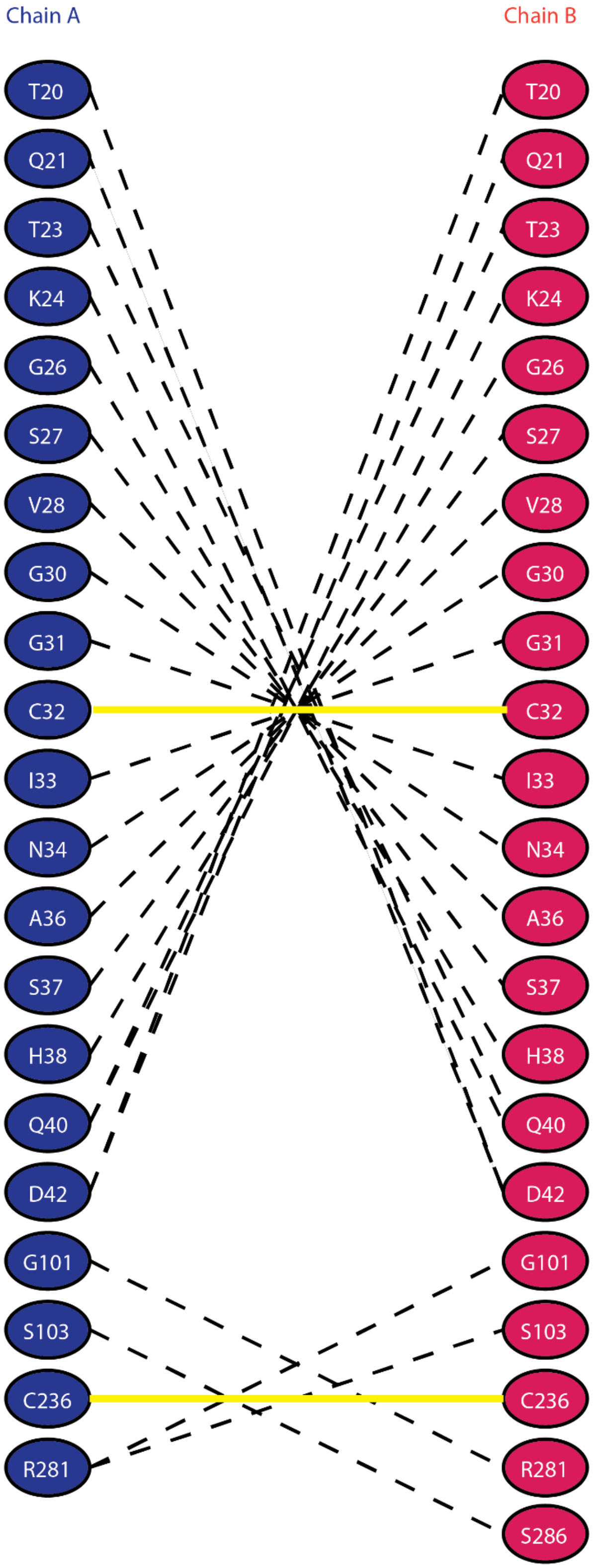

Fig. S1. Hydrogen bonds and disulfide bridges between chain A and chain B in AtFN3K WT. The hydrogen bonds between the chains are shown as black dashed lines and disulfide bridges between residues are shown as solid yellow lines. The hydrogen bonds were detected using PISA.

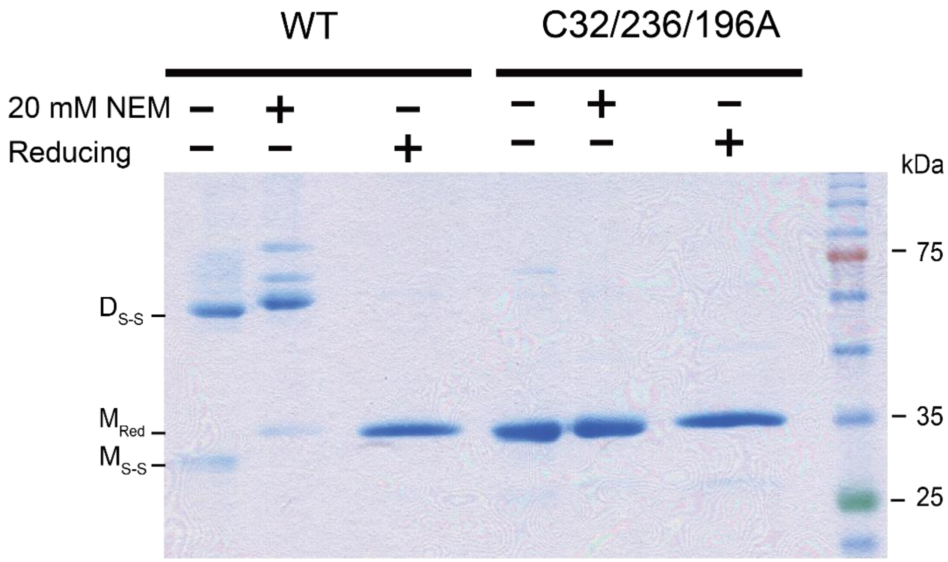

Fig. S2. Oxidized monomeric species are an artifact of the SDS-PAGE gel. SDS-PAGE of AtFN3K WT and triple cysteine mutant (Cys32Ala/Cys236Ala/Cys196Ala) dimer species. $D_{S\text{-}S}$: Disulfide linked dimer, M_{Red}: Monomer reduced, $M_{S\text{-}S}$: Monomer with intramolecular disulfide.

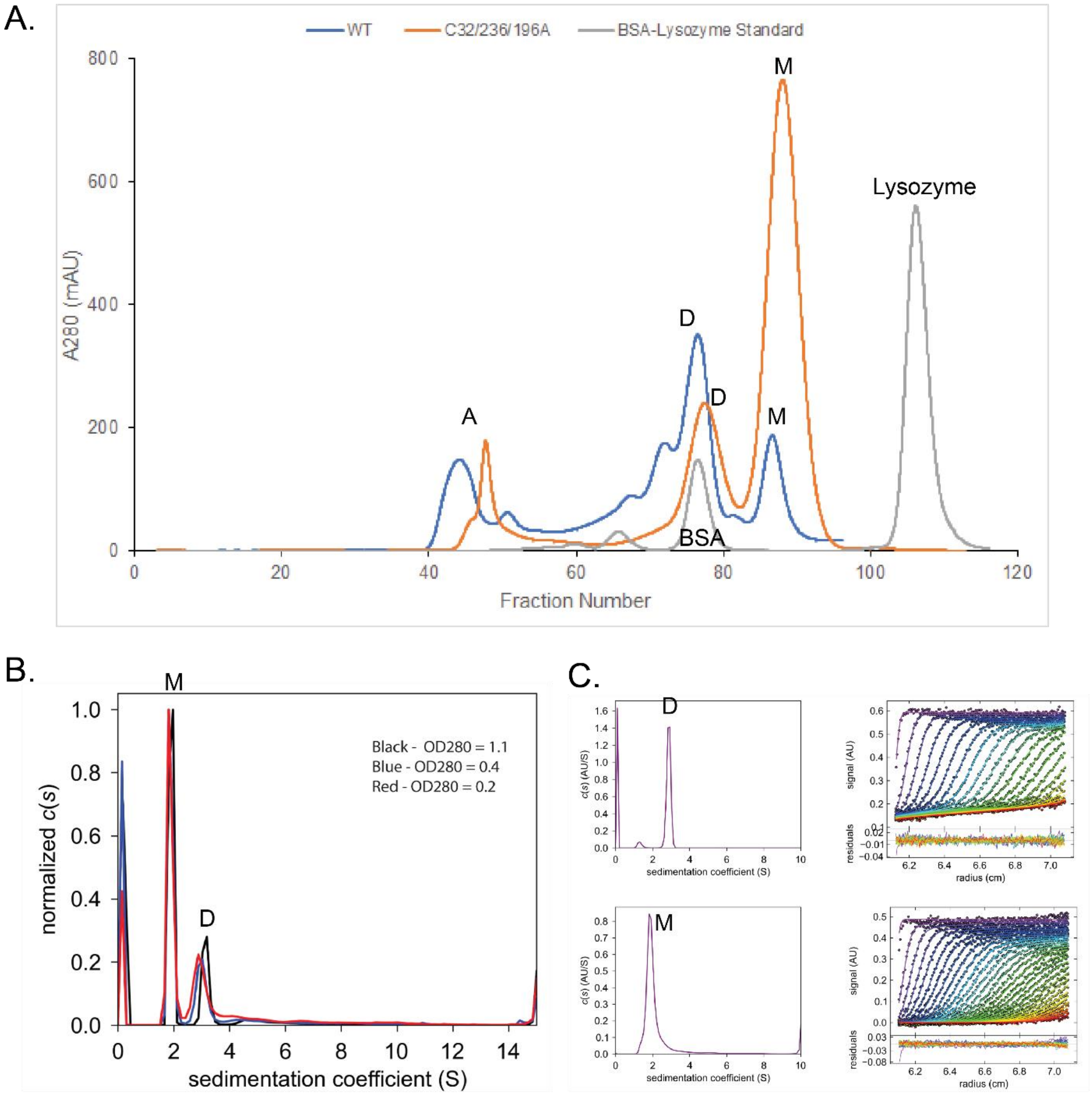

Fig. S3. WT and triple cysteine mutant (Cys32Ala/Cys236Ala/Cys196Ala) exist as two distinct species. (A) SEC of AtFN3K WT and the mutant overlaid with the SEC of BSA-Lysozyme mix. **(B)** Sedimentation velocity analysis of the triple cysteine mutant pre-SEC modeled as continuous c(s) distribution. Three different protein concentrations were used. **(C)**

Sedimentation velocity analysis of the triple cysteine mutant modeled as continuous c(s) distribution. Dimer and monomer fractions were isolated using SEC. (A, B, C) A: Aggregates, D: Dimer, M: Monomer. AtFN3K WT and triple cysteine mutants were purified without co-expression with GroEL.

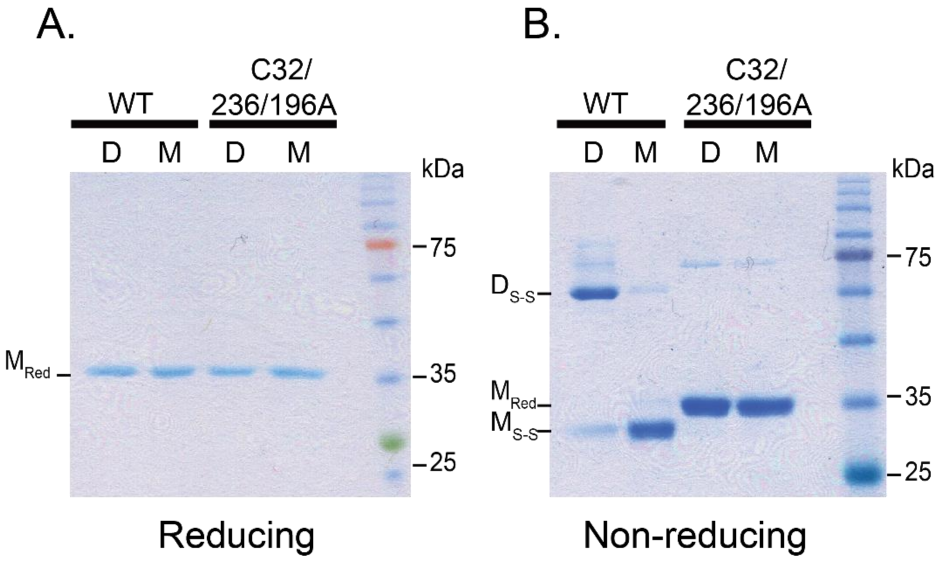

Fig. S4. Reducing and non-reducing SDS-PAGE of AtFN3K WT and triple cysteine mutant (Cys32Ala/Cys236Ala/Cys196Ala) dimer and monomer fractions. (A, B): D_{S-S}: Disulfide linked dimer; M_{Red}: Monomer Reduced; M_{S-S}: Monomer with intramolecular disulfide. Approximated 3 µg of protein was loaded. The gel was stained with Coomassie and de-stained with water.

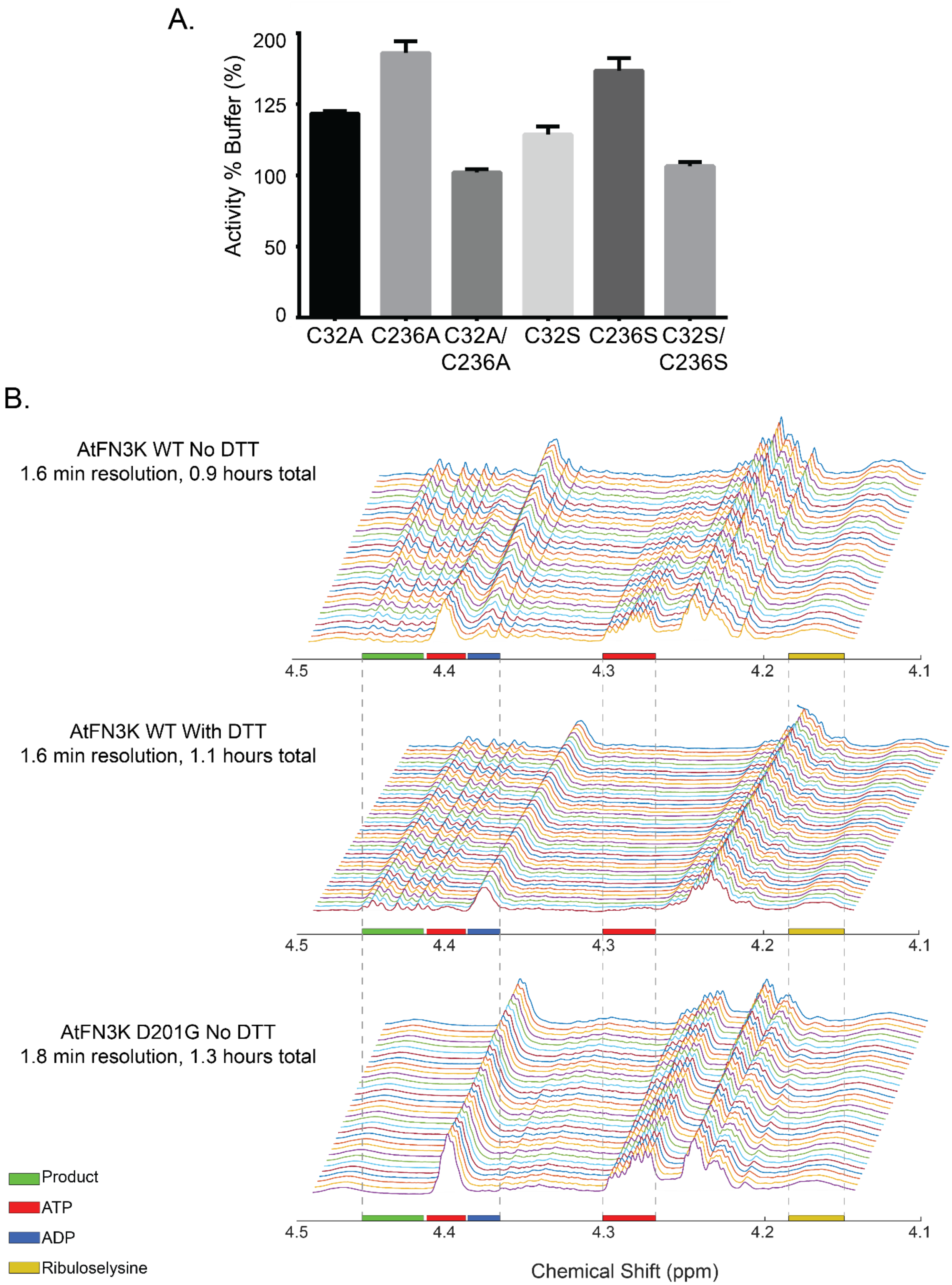
A.
Activity % Buffer (%)
200
125
100
50
0
C32A
C236A
C32A/ C236A
C32S
C236S
C32S/ C236S
B.
AtFN3K WT No DTT
1.6 min resolution, 0.9 hours total
AtFN3K WT With DTT
1.6 min resolution, 1.1 hours total
AtFN3K D201G No DTT
1.8 min resolution, 1.3 hours total
4.5
4.4
4.3
4.2
4.1
Chemical Shift (ppm)
🟩 Product
🟥 ATP
🟦 ADP
🟨 Ribuloselysine

Fig. S5. Effects of thiol reagents on activity of AtFN3Kand cysteine mutants. (A) PK/LDH assay of AtFN3K cysteine mutants. Error bars indicate the standard error of three independent experiments. Activity % Buffer is calculated by dividing activity in the presence of 2 mM DTT by activity in buffer alone and converting to percentage. **(B)** NMR spectrum showing the formation of product overtime for AtFN3K WT in the presence and absence of DTT. Kinase dead (Asp201Gly) is used as negative control. These assays were performed with purified protein without SEC. Because the purified proteins are a mixed population of active and inactive species, the fold change in activity is not comparable to the AtFN3K WT dimer isolated using SEC.

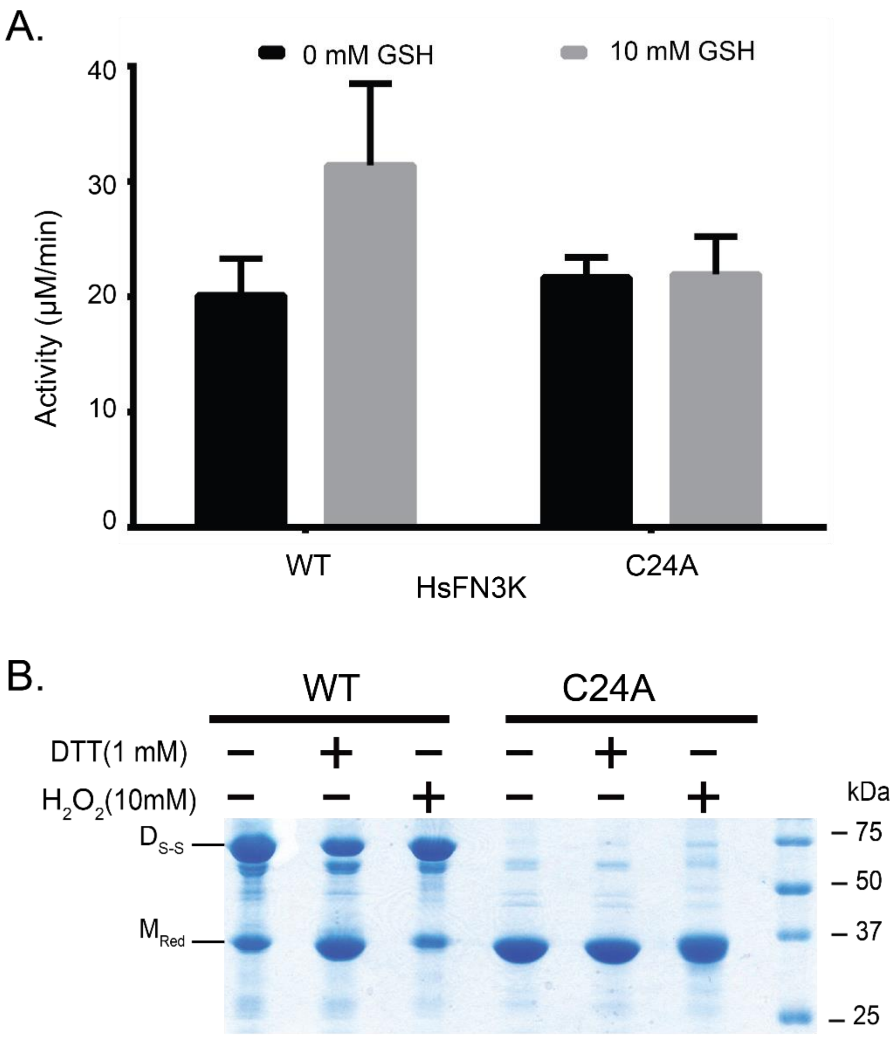

Fig. S6. P-Loop Cysteine (Cys^{24}) is critical for the formation of disulfide linked dimer in HsFN3K. (A) PK/LDH assay of HsFN3K WT and Cys24Ala in presence and absence of reduced glutathione (GSH). **(B)** Non-reducing SDS-PAGE of HsFN3K WT and Cys24Ala mutant. 15 µg of the recombinant protein was incubated with either water, 1 mM DTT or 10 mM H_2O_2 for half an hour before adding 4X Sample Buffer. The bands representing disulfide linked dimeric and monomeric species are labelled as $D_{S\text{-}S}$ and M_{Red} respectively. The gels were stained with Coomassie Brilliant Blue. The molecular marker is shown on the right.

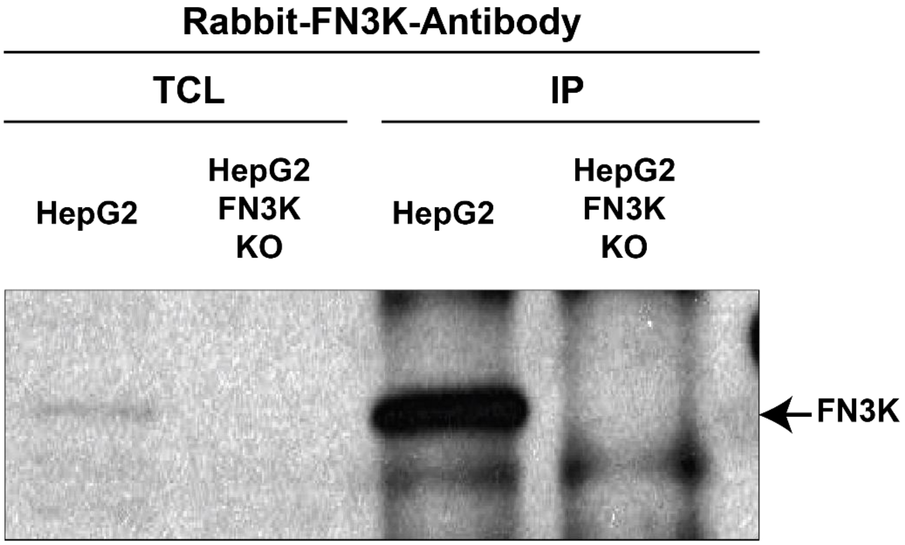

Fig. S7. Western blot of HsFN3K Knock Out (KO) in HepG2 cells. HepG2 (WT/KO) cells were lysed in lysis buffer (50mM Tris HCl pH 7.4, 100mM NaCl, 10% Glycerol, 1mM EDTA, 1% TritonX-100). Total cell lysate (TCL) was subjected to immunoprecipitation (IP) with anti-FN3K antibody. Proteins were resolved on 12% SDS PAGE gel and immunoblotted with Rabbit-FN3K antibody.

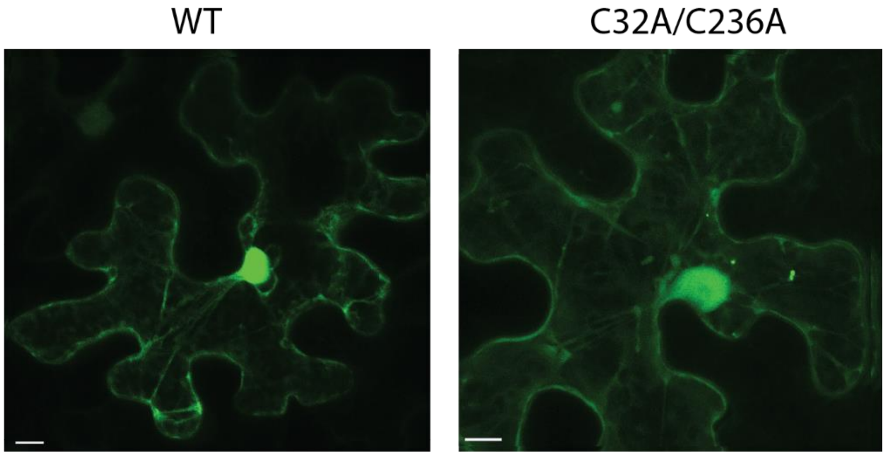

Fig. S8. WT and Cys32Ala/Cys236Ala AtFN3K localizes to the nucleus. Subcellular localization of AtFN3K WT and Cys32Ala/Cys236Ala respectively, in *N. benthamiana* leaf epidermal cells. Scale bar:10 μm.

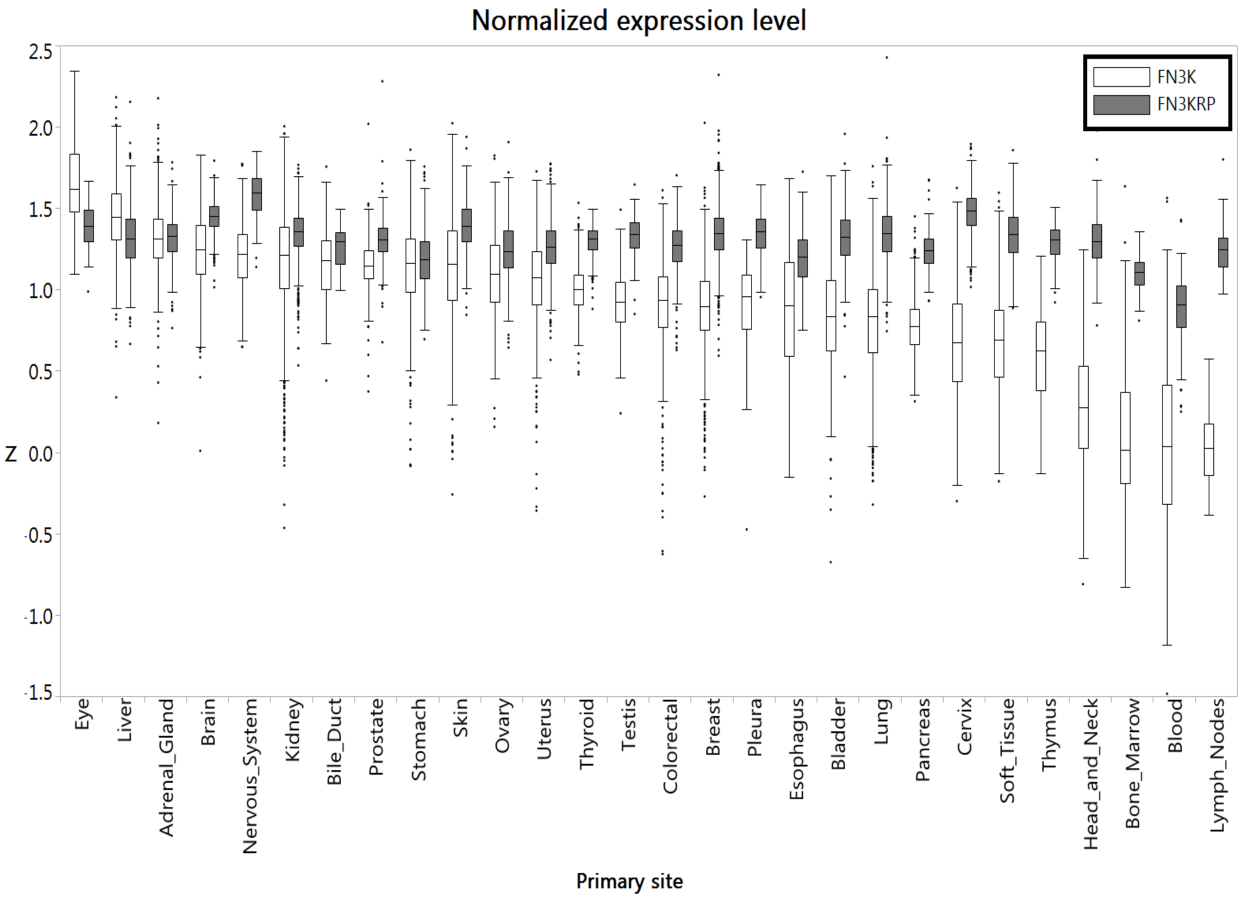

Fig. S9. Analysis of FN3K and FN3KRP expression in human tumors. Human tumor expression data (processed by upper quartile normalization) were obtained from GDC Data Portal (*73*). Expressions of FN3K and FN3KRP were then taken logarithm and standardized as z scores according to the mean and standard deviation of each sample. The boxplots show the z score distributions of FN3K (white boxes) and FN3KRP (gray boxes) in different tumor primary sites in descending order of the median z score of FN3K. Outliers are marked as dots.

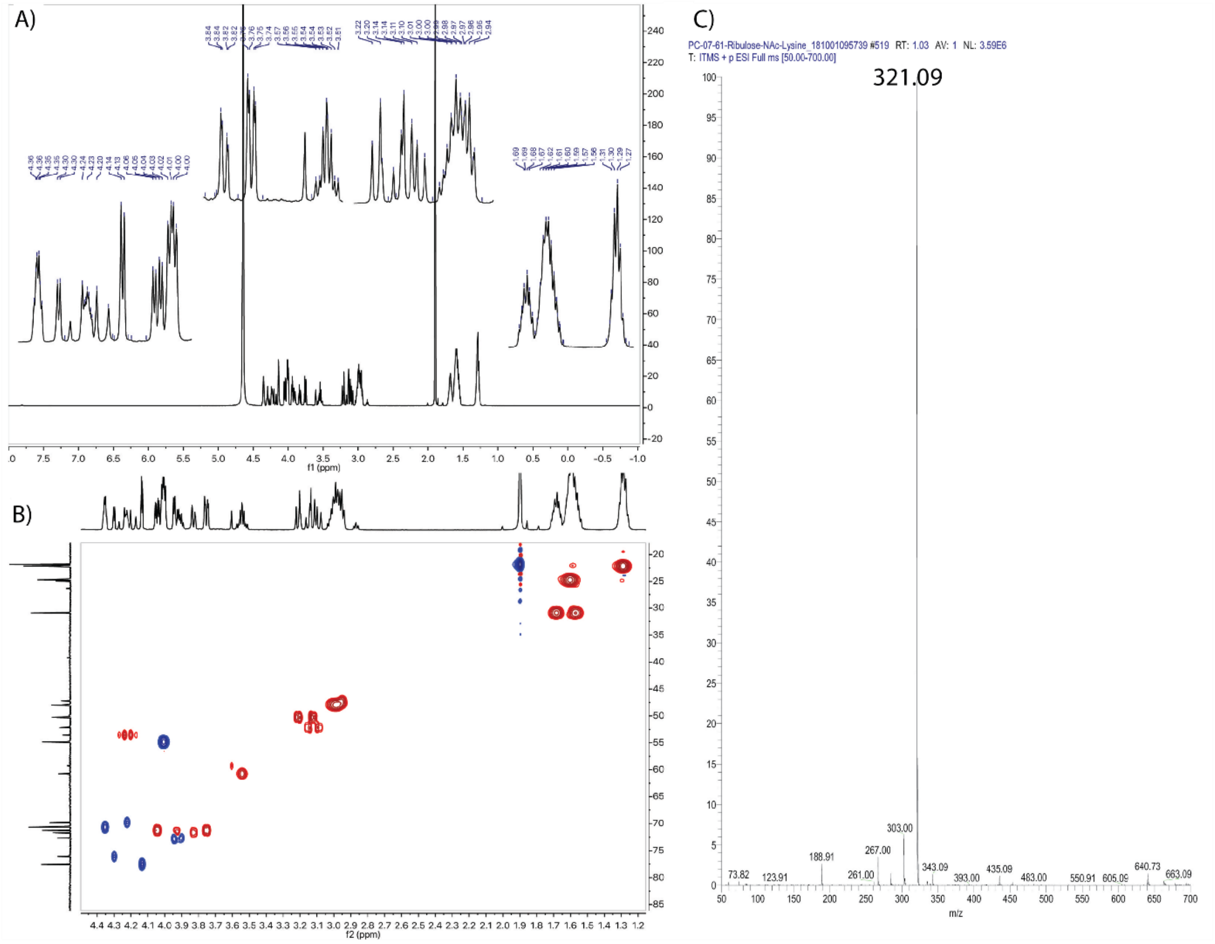

Fig. S10. Spectral data of Ribulose-N-α-Ac-lysine. (A) ^{1}H NMR (600MHz, D_2O) **(B)** HSQC (600MHz, D_2O) **(C)** LRMS (ESI-MS)

Data Collection	
Space Group	C 2 2 21
Unit cell dimensions (a, b, c, (Å) α, β, γ)	158.86 163.64 70.72 90.00 90.00 90.00
Total reflections	551252 (39245)
Unique reflections	38000 (2683)
Redundancy	14.5 (14.6)
Completeness (%)	1.00 (0.97)
I/σ(I)	14.3 (1.44)
R-meas[b] (%)	0.157 (2.50)
CC$_{1/2}$[c] (%)	0.999 (0.519)
Refinement	
Resolution (Å)	53.50 - 2.37
R_{work} / R_{free}	0.175 / 0.204
No. atoms Protein/Ligand/Water	4583/154/89
B-factors (Å^2) Protein/Ligand/Water	64.1/92.4/56.3
Stereochemical Ideality	
Bond lengths (Å^2)	0.009
Bond angles (°)	1.07
Ramachandran favored (%)	97
Ramachandran allowed (%)	3
Ramachandran outliers (%)	0

[a] Values in parentheses are for highest-resolution shell.

[b] R_{meas} is the redundancy independent merging R-factor of Diederichs and Karplus (*74*)

[c] $CC_{1/2}$ is the percentage of correlation between intensities from random half-data sets (*75*)

Table S1. Data collection and refinement statistics of WT AtFN3K.

Metabolite	**Mean and SE**				**Fold Change KO vs WT**	**FDR-corrected *p*-value**
	WT		**FN3K-KO**			
Glycine	1.655	0.029	1.152	0.043	-0.304	4.50E-07
Serine	0.976	0.022	0.754	0.024	-0.227	2.82E-05
Formate	0.080	0.002	0.059	0.002	-0.267	2.82E-05
Aspartate	0.417	0.012	0.333	0.010	-0.202	3.17E-04
Glutathione	0.422	0.019	0.565	0.022	0.339	0.001
Panothenate	0.390	0.006	0.353	0.005	-0.095	0.001
Creatine	0.608	0.016	0.725	0.026	0.192	0.004
Thioacetamide	0.124	0.006	0.153	0.004	0.238	0.004
Putrescine	0.146	0.005	0.168	0.003	0.147	0.005
UDP GlcNAc	0.050	0.002	0.035	0.003	-0.289	0.006
Lactate	1.598	0.118	2.112	0.089	0.321	0.007
Glycerophosphocholine	0.615	0.012	0.535	0.021	-0.130	0.008
Lysine	0.136	0.005	0.152	0.002	0.119	0.015
Phosphocreatine	0.670	0.019	0.583	0.024	-0.130	0.017
Keto-methylvalerate	0.117	0.005	0.134	0.003	0.149	0.023
Threonine	0.967	0.017	1.061	0.034	0.097	0.029
Proline	0.114	0.002	0.124	0.004	0.089	0.039
Glutamine	0.265	0.004	0.286	0.009	0.079	0.043
Valine	0.537	0.016	0.518	0.017	-0.036	0.528
Leucine	0.879	0.037	0.845	0.038	-0.038	0.638
Glutamate	1.116	0.023	1.096	0.037	-0.018	0.740
Citrate	0.225	0.005	0.223	0.004	-0.008	0.854
Glucose	0.081	0.020	0.074	0.021	-0.084	0.854
Alanine	2.788	0.086	2.793	0.103	0.002	0.974

Table S2. Metabolites identified in extracts of WT HepG2 and FN3K-KO cells.